Isolating large-scale smoke impacts on cloud and precipitation processes over the Amazon with convection permitting resolution

Ross Herbert[1], Philip Stier[1], Guy Dagan[1]

[1] Atmospheric, Oceanic and Planetary Physics, Department of Physics, University of Oxford, Oxford, UK

Corresponding author: Ross Herbert (ross.herbert@physics.ox.ac.uk)

Key Points

- Smoke drives strong diurnal responses in convection, cloud cover, and precipitation that cannot be observed by polar-orbiting satellites.
- The radiative effect of smoke is sensitive to plume longevity and the response of high-altitude clouds that exert a strong positive effect.
- Simulations suggest the localized suppression of convection scales with the optical depth of smoke over the Amazon rainforest.

Abstract

Absorbing aerosol from biomass burning impacts the hydrological cycle and fluxes of radiation both directly and indirectly via modifications to convective processes and cloud development. Using the ICON model in a regional configuration with convection-permitting resolution of 1500 m, we isolate the response of the Amazonian atmosphere to biomass burning smoke via enhanced cloud droplet number concentrations N_d (aerosol-cloud-interactions; ACI) and changes to radiative fluxes (aerosol-radiation-interactions; ARI). We decompose ARI into contributions from surface cooling (reduced surface shortwave flux) and localized heating of the smoke layer. We show that ARI influences the formation and development of convective cells: surface cooling below the smoke drives suppression of convection that increases with the smoke optical depth, whilst the elevated heating promotes initial suppression and subsequent intensification of convection overnight; a corresponding diurnal response from high precipitation rates is shown. Enhanced N_d (ACI) perturbs the intensive cloud properties and suppresses low-to-moderate precipitation rates. Both ACI and ARI result in enhanced high-altitude ice clouds that have a strong positive longwave radiative effect. Changes to low-cloud coverage (ARI) and albedo (ACI) drive an overall negative shortwave radiative effect, that slowly increases in magnitude due to a moistening of the boundary layer. The overall net radiative effect is dominated by the enhanced high-altitude clouds, and is sensitive to the plume longevity. The considerable diurnal responses that we simulate cannot be observed by polar orbiting satellites widely used in previous work, highlighting the potential of geostationary satellites to observe large-scale impacts of aerosols on clouds.

Plain Language Summary

There remain important uncertainties on how smoke from forest and grassland fires impacts the past, present, and future climates. In this study we use a detailed model of the atmosphere over the Amazon rainforest to understand and quantify the processes by which smoke influences clouds and rain via two pathways: the first driven by changes to the absorption of solar radiation through the smoky atmosphere, and the second driven by an increase in the number of cloud droplets due to smoke particles. We find that the diurnal cycle of convection that drives much of the Amazon rainfall is greatly affected by changes to the radiation with less activity during the day and increasing activity overnight. The more numerous cloud droplets make the clouds brighter and help suppress rainfall rates. Changes to both radiation and cloud droplet number results in more extensive and thicker ice-phase clouds that exert a warming effect on the climate; the longer the smoke plume persists for, the stronger the warming effect. Our findings highlight important processes that are not sufficiently represented in global climate models, and also highlight a need to use time-resolved geostationary satellite observations of the region to capture more of the diurnal cycle.

1 Introduction

Airborne aerosol particles, such as sea salt, mineral dust, or carbonaceous material, impact our climate via interactions with solar and terrestrial radiation (known as aerosol-radiation interactions; ARI) and via their

ability to act as cloud condensation nuclei (known as aerosol-cloud interactions; ACI). Wildfires occur annually in many tropical regions across the globe (e.g., the Amazon, central Africa, Borneo) and often cover vast areas with highly perturbed loadings of aerosol that can persist for weeks to months. These plumes are able to transport the carbonaceous biomass burning aerosol (BBA) high into the atmosphere and far from the source (Holanda et al., 2020), demonstrating the potential for widespread non-local impacts. BBA influences the environment via both ARI and ACI. The strongly absorbing optical properties of BBA result in an instantaneous localized heating of the plume and a reduction in surface solar radiation. BBA also act as cloud condensation nuclei (CCN) and therefore have the potential to enhance the cloud droplet number concentration (N_d). The potential for BBA to have far-reaching and prolonged impacts on radiation and cloud cover, coupled with remaining uncertainties in BBA optical and physical properties, has resulted in BBA being identified as a key source of uncertainty in future projections of the climate (Bond et al., 2013; Boucher et al., 2013).

The Amazon region is the world's largest forested region, representing a vast store of carbon and playing an important role in the world's hydrological cycle (Lovejoy & Nobre, 2019). Wildfires in the Amazon forest and the surrounding savannah coincide with the dry season (August to October) and may become more numerous under drought conditions (Aragão et al., 2007; Ten Hoeve et al., 2012). Future climate projections predict an increase in the frequency and intensity of drought events (Stocker et al., 2013), and a lengthening of the dry season (Boisier et al., 2015), both of which may enhance fire activity. Additionally, in the past decades anthropogenic activities, mainly from large-scale clearing and burning for agriculture, have greatly impacted the number and scale of fires in the region (Morton et al., 2008) and have resulted in an increase in savannah grassland at the expense of forest cover (Nobre et al., 2016). A recent upward trend in deforestation (Oliveira et al., 2020) highlights both recent increases in fire activity, but also substantial variation in decadal deforestation trends.

Observations made at field sites across the Amazon suggest precipitation is suppressed by the presence of BBA alongside intensification in certain conditions. Andreae et al. (2004) report evidence of smoke reducing the size of cloud droplets, delaying and elevating the onset of precipitation, and increasing the vertical extent of clouds. An overall suppression of the warm rain process was observed using a ground-based radar at Manaus (Gonçalves et al., 2015), though some intensification of convection was observed in more unstable atmospheres. Camponogara et al. (2014) and Bevan et al. (2008) also observed correlations between aerosol optical depth (AOD) and the suppression of precipitation at several ground sites across the Amazon. The spatial extent of the Amazon and associated BBA plumes necessitates the use of spaceborne retrievals to examine BBA impacts on the larger-scale environment. Kaufman and Nakajima (1993) found that increases in AOD coincided with warmer cloud tops (lower altitude) pointing towards a suppression of convection instead of invigoration; this conclusion was also reported by Jiang et al. (2018). Koren et al. (2008) reported that at low loadings (below AOD of ~ 0.3) low cloud cover increases with AOD, but decreases at higher loadings and Ten Hoeve et al. (2011) reported a similar relationship for cloud optical depth. These relationships may however occur in part due to confounding factors such as meteorology (Gryspeerdt et al., 2017; Yu et al., 2007). The previously listed satellite-based studies have a local overpass time of ~ 1330 local solar time (LST), which poses the question as to whether these observations are representative of the full diurnal response of the cloud to BBA.

Modelling studies have been performed on a range of resolutions and domain sizes over the region and highlight some key impacts to the large-scale environment. BBA reduces surface fluxes (Zhang et al., 2008) that can directly lead to reduced cloudiness (Feingold et al., 2005) and promote a stabilization of the boundary layer (BL) via surface cooling and heating aloft (Liu et al., 2020; Zhang et al., 2009). The changes to the thermodynamic structure of the BL can have widespread impacts on circulation and moisture transport (Lee et al., 2014; Yu et al., 2007; Zhang et al., 2008, 2009), the suppression of convection at the surface (Liu et al., 2020; Martins et al., 2009; Wu et al., 2011), and potentially enhance convection aloft (Wu et al., 2011). Generally, these studies suggest that cumulative precipitation in the dry season decreases due to smoke presence (Liu et al., 2020; Martins et al., 2009; Thornhill et al., 2018; Wu et al., 2011) but peak intensities may increase (Martins et al., 2009). There is less agreement as to how liquid water path (LWP), ice water path (IWP), and cloudiness responds, which may be due to the differing mechanisms by which ARI and ACI impact cloud formation and evolution. One such mechanism, referred to as CCN-induced

cloud invigoration, links an increase in CCN with an increase in buoyancy and convective cloud updraft speed, which may occur via enhanced condensation of cloud droplets or enhanced flux of condensate to the freezing level (e.g., Fan et al., 2018; Khain et al., 2005; Lebo, 2018; Rosenfeld et al., 2008). The lack of consensus amongst modelling studies has implications for the overall radiative effect of BBA. Generally, an increase in low-cloud cover cools the climate, whereas an increase in high-cloud cover warms the climate. Without a consensus on the direction of the response from these cloud types it is difficult to quantify the role of BBA in the earth-system.

In this modelling study we aim to isolate the response of the clouds, precipitation, and larger-scale environment to BBA from microphysical effects (ACI) and radiative effects (ARI). We then further decompose ARI to focus on the roles of surface cooling (due to a reduction in downwelling shortwave radiation) and in-situ heating of the BBA layer. We use a large domain (3000 x 2000 km) with high spatial resolution (1.5 km) that resolves the diurnal cycle of convection and permits the full evolution of mesoscale convective systems across the Amazon. We also use a semi-idealized treatment of the BBA plume, grounded by observations, to reduce the uncertainty that arises from the aerosol distribution and evolution. The results will highlight the important diurnal response of clouds and precipitation and the processes that drive them, whilst allowing us to identify important gaps in our knowledge and help understand conflicting observations and results in other modelling studies. The remainder of the paper is set out as follows. In Section 2 we briefly describe the atmospheric model that is being used for this study along with the setup of the domain, then describe the representation of aerosol effects in the model, and outline the experiments being performed. In Section 3 we present the main results of our study starting with a stepwise focus on the domain response in each experiment, followed by the top-of-atmosphere radiative effects, and then we examine the relationship between BBA optical depth and the suppression of convection. Finally, in Section 4 we put our results into a broader context and provide a comparison with other studies, before concluding the study.

2 Methodology

2.1 Model description and setup

We use the ICOahedral Non-hydrostatic (ICON) atmospheric model in a regional, limited-area, configuration; a full description and evaluation of the model is provided by Zängl et al. (2015). This setup has been used in previous studies (Dagan et al., 2020; Klocke et al., 2017) to study clouds and aerosol-cloud interactions. The model domain, covering an area of ~6 x 10^6 km^2, is centered on the Amazon between longitudes 68°W to 4°W and latitudes 15°S to 3°N (Figure 1) on a triangular grid with a horizontal resolution of ~1500m, which is able to represent convection without the need for sub-grid scale parameterizations of mid-level and deep convection (Klocke et al., 2017). We use the terrain-following Smooth Level Vertical SLEVE coordinate system (Leuenberger et al., 2010) in the vertical, with 75 levels extending up to an altitude of 30 km. Radiation is represented interactively using the Rapid Radiative Transfer Model for GCMs (RRTM-G) that operates on 16 longwave bands and 14 shortwave bands (Iacono et al., 2008; Mlawer et al., 1997). Cloud microphysical processes are represented using the double-moment microphysics scheme of Seifert & Beheng (2006) that predicts the mass and number evolution of five hydrometeor species; microphysics and radiation schemes are coupled via the cloud droplet effective radius that is calculated in the former. The exchange of heat, moisture, and momentum fluxes at the surface are interactively represented using the TERRA interactive surface scheme (Schrodin & Heise, 2002).

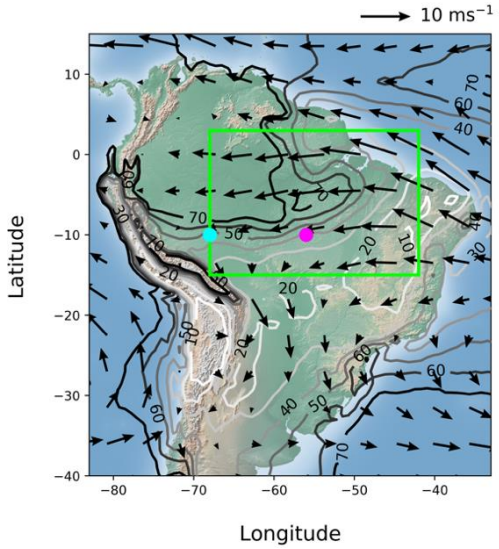

Figure 1. September climatology of 850 hPa winds (arrows; scale shown above the plot) and total cloud fraction (contours; labelled as percentages) from the ERA-Interim reanalysis dataset (2000 to 2018) over the Amazon rainforest. The green box shows the boundaries of the model domain used in this study. The pink and cyan points show the locations of the Alta Floresta and Rio Branco AERONET sites, respectively.

ERA5 reanalysis (ERA5, 2017) is used for initialization of the model and for boundary conditions that are supplied every 6 hours throughout the simulation and linearly interpolated between the time intervals. All simulations are run for 8 days with a model time step of 12 seconds; 3D fields are output every 3 hours and 2D surface fields output hourly. The simulations are initialized at 0000 UTC on 31 August 2007 and run until 0000 UTC 8 September 2007. This date coincides with a prolonged period of elevated AOD over the Amazon during the dry season, shown in the Aerosol Robotic Network (AERONET; Holben et al., 2001) measurements of AOD in Figure 2.

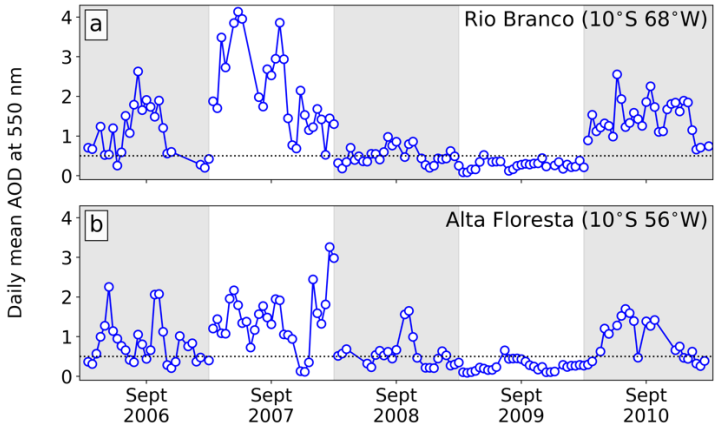

Figure 2. Monthly timeseries of daily mean aerosol optical depth (AOD) during September measured at AERONET stations at **a** Rio Branco (10°S 68°W) and **b** Alta Floresta (10°S 56°W) from 2006 to 2010 (locations shown in figure 1). The horizontal dotted line highlights an AOD of 0.5.

2.2 Representation of aerosol effects

The horizontal and vertical distribution of aerosol is represented using the Max Planck Institute Aerosol Climatology version 2 - Simple Plume model (MACv2-SP; Stevens et al., 2017). MACv2-SP allows the user to prescribe a number of idealized radiatively active plumes each with a prescribed location, spatial structure, vertical profile, annual cycle, AOD at plume center (given at 550 nm), single scattering albedo (SSA), asymmetry parameter (given at 500 nm), and angstrom exponent. In our simulations we isolate the 'South America' plume and prescribe parameters as set in Stevens et al. (2017) except for the AOD and SSA (see table 1 in Stevens et al., 2017). The resulting vertical and horizontal distribution of aerosol is shown in Figures 3a and 3b. The plume location and horizontal extent are in good agreement with a climatology presented by Malavelle et al. (2019); the plume center is at 62°W 10°S and decreases towards the north and

east, with background AOD values < 0.1 at the Atlantic coast. MACv2-SP places much of the BBA plume within the lower 2 or 3 km of the atmosphere with a peak at ~ 0.5 km altitude (Figure 3a) which is in agreement with observations (Andreae et al., 2004; Gonzalez-Alonso et al., 2019; Reddington et al., 2019).

Two setups using the MACv2-SP model were used to represent the radiative effect of aerosol. The first is the standard representation of biomass burning aerosol, with a maximum AOD of 1.5 and an SSA of 0.87, which results in localized heating of the aerosol layer and a reduced surface flux of shortwave (SW) radiation. This peak AOD is within sustained magnitudes observed during this period (Figure 2a; see also Schafer et al., 2008) and only represents a small region of the domain (Figure 3b). The second setup is designed to only represent the reduced downward surface SW flux and associated surface flux changes. Increasing the SSA to 1.0 removes the localized heating but simultaneously enhances the SW diffuse component reaching the surface; the result is a weaker reduction in surface SW flux when compared to the first setup. In order to achieve a consistent SW reduction at the surface the AOD was increased by a factor of 2.55 (determined using SOCRATES: Suite of Community Radiation Codes based on Edwards & Slingo, 1996). This results in an unrealistically high AOD but for this experiment we are only concerned with the effect that the changes to the surface fluxes have on the evolution of the domain.

The MACv2-SP model includes a parameterized ACI effect that represents the enhancement of N_d due to increased anthropogenic aerosol. The parameterization presented by Stevens et al. (2017), and shown in Figure 3c (dashed line), is based on a mean climatology of N_d and AOD retrieved by MODIS over the ocean. As will be shown below, observations of N_d from campaigns throughout the Amazon routinely report N_d exceeding 100 cm^{-3} and indeed this maximum, as reflected by the parameterization, may be better suited as a minimum background value for the region. Therefore, the current MACv2-SP parameterization, which may well be representative of large-scale perturbations over marine environments, is not suitable for our region of interest.

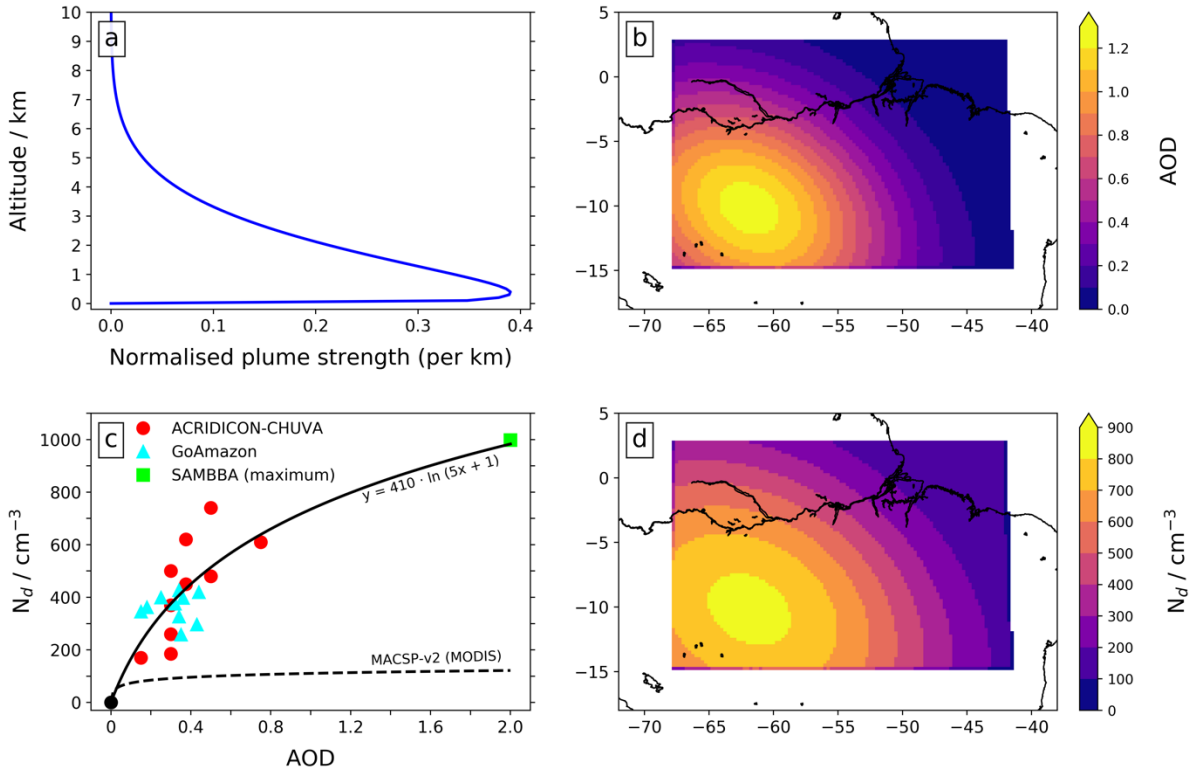

Figure 3. Prescribed vertical (**a**) and horizontal (**b**) distribution of AOD from the MACv2-SP plume model; relationship between N_d and AOD (**c**); and horizontal distribution of the N_d (**d**). In **c** the different symbols correspond to in-situ measurements of N_d from three different field campaigns (see manuscript for further details); the solid black line shows the observationally-informed N_d-AOD relationship used in this study and the dashed line shows the original relationship in MACv2-SP for reference.

In our simulations we represent the enhancement of N_d due to BBA using a relationship between AOD and N_d based on in-situ measurements made during three campaigns over the Amazon. We stress that we are not presenting a new parameterization, but rather producing a realistic relationship that allows us to explore the impact of enhanced N_d to the simulated domain in an idealized setup. The goAMAZON campaign (Martin et al., 2016) took place at Manaus and included localized flights during the dry season. Mean values of N_d for each flight (10^{th} to 90^{th} percentile of data above 1 cm^{-3}) were determined using in-situ measurements of N_d from the CDP and 2DS probes (https://www.arm.gov/research/campaigns/amf2014goamazon), and corresponding values of AOD taken from the Manaus AERONET station. The ACRIDICON-CHUVA campaign (Wendisch et al., 2016) included flights that extended over much of the Amazon. Median N_d measured during the flights are presented by Polonik et al. (2020) and used here. AOD measurements were taken from AERONET stations either at Manaus or Alta Floresta, depending on availability and proximity to the flight. The SAMBBA campaign (details in Brito et al., 2014 and Darbyshire et al., 2019) was based at Porto Velho with flights extending over much of the Amazon. In-situ measurements from the CDP probe (http://data.ceda.ac.uk/badc/sambba/data) were used to determine flight-mean values of N_d (10^{th} to 90^{th} percentile of data above 1 cm^{-3}). Due to reservations on the quality of data we only use the maximum SAMBBA value of ~ 1000 cm^{-3} (flight b742) to inform our relationship; this value is within the upper range as observed by Polonik et al. (2020). This maximum N_d is combined with a maximum AOD of 2.0, which lies within sustained AOD measurements shown in Figure 2 and in other observations (Schafer et al., 2008).

The data from the campaigns are plotted in Figure 3c along with a logarithmic function (following Stevens et al., 2017) that describes the combined datasets:

$$N_d = 410\ \ln(5\tau + 1), \qquad \text{Equation 1}$$

where N_d is in cm^{-3} and τ is the dimensionless AOD. The new relationship displays much more sensitivity of N_d to AOD than the MACv2-SP parameterization. Applying the new relationship to the horizontal AOD distribution from the MACv2-SP model (Figure 3b) provides a horizontal distribution of prescribed N_d (Figure 3d) that we couple to the cloud microphysics scheme. This idealized treatment of aerosol and N_d sacrifices some realism in that the distribution of both would naturally evolve both spatially and temporally, but allows us to reduce the uncertainty that the complexity of aerosol microphysics processes and aerosol activation would add to understanding aerosol-cloud-radiation interactions (Gryspeerdt et al., 2017; Rothenberg et al., 2018; Simpson et al., 2014). Additionally, we routinely see sustained periods (weeks to months) of enhanced BBA over the Amazon (see Figure 2) which would provide a continuous source of aerosol and CCN, so our simulations could be seen as a proxy for these prolonged periods of BBA.

2.3 Experiments

We perform five simulations using the same initial meteorological and lateral boundary conditions. A list of experiments is shown in Table 1. In *CONTROL* we use background distributions of AOD and N_d to produce a control simulation to compare with the remaining experiments. Based on the lowest values measured during field campaigns in the region we use a background N_d of 100 cm^{-3} which equates to a background AOD (using Equation 1) of 0.06. In the *MPHYS* experiment we only perturb the N_d distribution (see Figure 3d); this allows us to focus on the response of the domain to changes in N_d induced by the BBA and is analogous to the ACI effect. In the *RAD* experiment only the 3D aerosol distribution in the radiation scheme is perturbed (Figures 3a and 3b) whilst N_d is kept at the background value; we use this to isolate the radiative effect of BBA which results in perturbations to the temperature profile and is analogous to the ARI effect. Using this method, the semi-direct effect (Herbert et al., 2020; Johnson et al., 2004) is implicitly included in ARI effects. The *RAD-scat* experiment is similar to *RAD* but here the SSA has been increased to 1.0 and the AOD enhanced by a factor of 2.55 (see Section 2.2 for details); this allows us to isolate the impact of SW radiative effects on surface fluxes. For the *TOTAL* experiment we perturb both the N_d and aerosol distribution to see the total effect of BBA on the domain.

Table 1. Details of the experiments being performed in this study. All simulations are performed for 8 days with the same initial conditions and lateral boundary conditions.

Experiment name	Details
CONTROL	Background AOD (0.06) and N_d (100 cm^{-3}) distribution
MPHYS	Perturb N_d distribution only: *isolate microphysical effect of BBA on N_d*
RAD	Perturb AOD distribution only: *isolate full radiative effect of BBA*
RAD-scat	As RAD experiment but with SSA of 1.0: *isolate radiative effect of BBA at surface only*
TOTAL	Perturb both AOD and N_d distribution: *full radiative and microphysical effects from BBA*

3 Results

3.1 Characteristics of the control simulation and comparison with observations

We begin by describing the characteristics of the control simulation and compare with observations that show the model is reproducing a realistic diurnal cycle. **Figure 4** shows the domain during a diurnal cycle, starting in the afternoon of day 3 and progressing throughout the evening and night. At 1400 local solar time (LST) the LWP exceeds 100 gm^{-2} in numerous small-scale features (Figure 4a) consistent with thermally triggered convective cells. The cells are advected westward and aggregate, producing larger mesoscale cells that continue to develop throughout the night (Figures 4b – d). Extensive regions of stratiform cloud with low LWP are present over the coastal regions to the northeast of the domain and downwind of the convection in the northwest. Precipitation (Figures 4e – h) coincides with regions of high LWP and convective activity, with extensive small-scale features present at 1400 LST that grow to larger, more isolated, cells during the evening and overnight. Maximum (99^{th}-percentile) precipitation rates in the convective cells reach 22 mm hr^{-1} at 1400 LST and drop to 16 mm hr^{-1} at 0200 LST. The convection lofts condensate to the freezing level and produces extensive high altitude ice clouds which can be seen predominantly in the northwest of the domain (Figures 4i – l and Figures 4m – p) with ice-water path (IWP) exceeding 260 g m^{-2} in some regions. These clouds appear more extensive at 2000 LST (Figure 4n) and dissipate overnight, reflecting the time required for the convective cells to grow large enough to penetrate into the upper troposphere.

Figure 5 shows mean precipitation rates across the domain from satellite-based estimates (IMERG data product 3B-HHR-E.MS.MRG.3IMERG V06B; Huffman et al., 2019) and the simulation for the same time period (31 Aug to 6 Sept 2007). The satellite-based estimates show a distinct diurnal cycle with a peak between 1400 and 1500 LST and a second, more variable, peak during the night at ~0500 LST. The afternoon peak is driven by deep convection, and the overnight peak by mesoscale systems that develop within the domain or are advected into the domain. Our control simulation is able to reproduce the timing and the general characteristics of the diurnal cycle of precipitation. We see the largest peak between 1400 to 1500 LST and a second peak with more variability during the night. The simulation generally produces a lower precipitation rate than the IMERG dataset, though this could be due to an over-estimation of moderate (0.4 – 10 mm hr^{-1}) rainfall rates in IMERG that have been reported over the Amazon (Oliveira et al., 2016).

These results demonstrate that the ICON model and our configuration is able to reproduce the observed characteristics of the diurnal cycle of convection and precipitation over the Amazon basin, and provides a reliable control simulation for understanding BBA plume impacts on the domain.

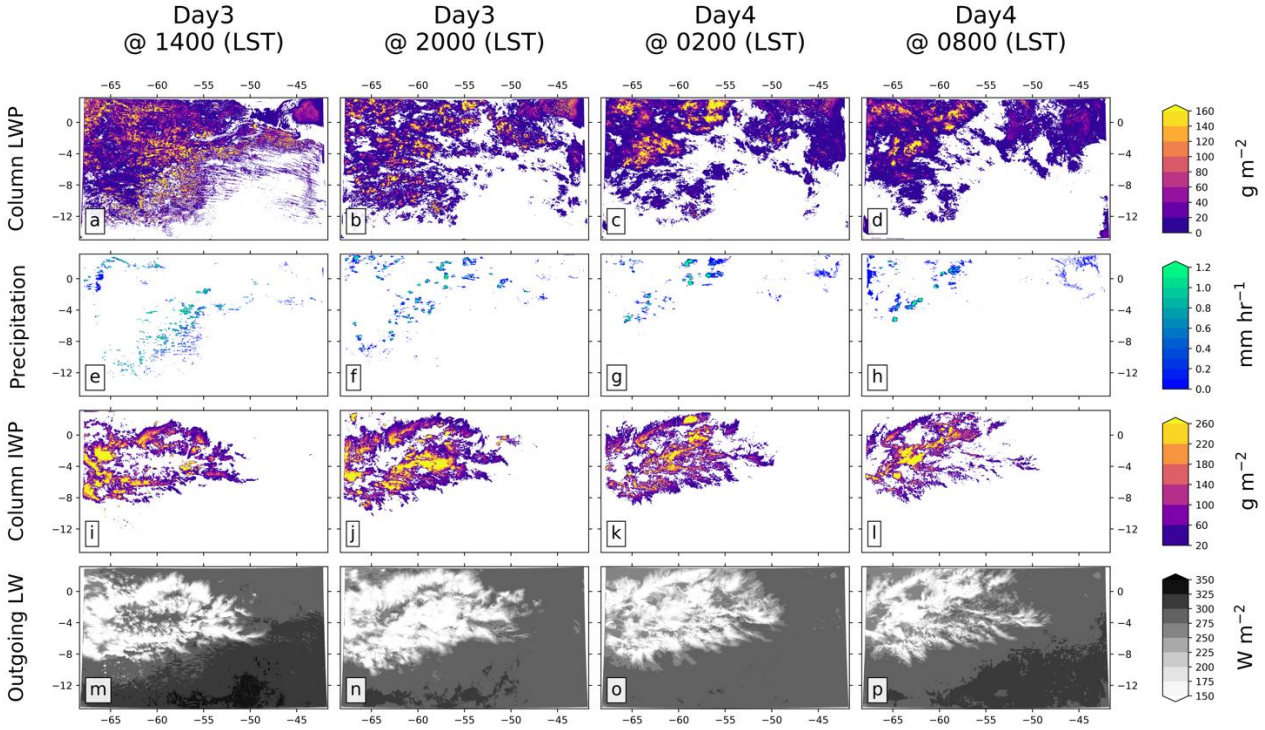

Figure 4. Evolution of the domain in the control simulation with instantaneous values of column liquid-water path (**a** – **d**), precipitation rate (**e** – **h**), column ice-water path (**i** – **l**), and top-of-atmosphere outgoing LW flux (**m** – **p**). Output is shown for 1400, 2000, 0200, and 0800 local solar time (LST) over days 3 and 4.

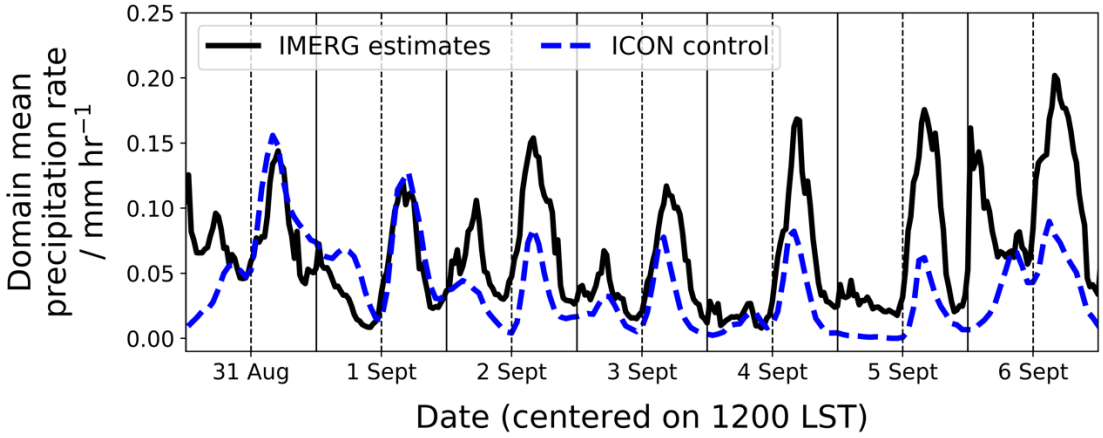

Figure 5. Comparisons of the simulation with observations. Timeseries of the mean precipitation rate over the model domain (see Figure 1) throughout the simulated time period (year 2007) from IMERG satellite-based estimates (solid black line) and the control simulation (dashed blue line). Vertical dashed (solid) lines are at 1200 (0000) local solar time for each day.

3.2 Response to perturbations

3.2.1 *MPHYS* experiment

Increasing N_d in the *MPHYS* experiment (see table 1) strongly suppresses precipitation in the initial stages (days 1 and 2) throughout the domain at all precipitation intensities (Figure 6b), accompanied by an increase in the domain mean LWP (Figure 7c) of ~10 g m^{-2} (~20 %). This is driven by a shift of the cloud droplet distribution to smaller sizes (Figure 9c) which suppress the warm rain process (Albrecht, 1989; Heikenfeld et al., 2019; Xue et al., 2008). The enhanced liquid condensate and smaller droplets reduce surface downwelling radiation, and removes a source of water vapor and evaporative cooling below the cloud base. The consequence is enhanced convective inhibition and an overall weakening of moderate updrafts ($w_{max} \leq 5$ m s^{-1}) in the initial response (Figure 8b). In the same time period, there is no significant change in the fraction of the domain covered by liquid cloud (Figure 9a), demonstrating the initial response of the domain to an N_d perturbation primarily impacts the intensive cloud properties, rather than the thermodynamic

properties that drive cloud formation. The LWP histogram (Figure 7c) shows a decrease at 100 g m^{-2} and an increase at 1000 g m^{-2} on day 1, attributed to a deepening of clouds at the expense of shallow clouds, which supports this hypothesis. A second consequence of enhanced N_d in the *MPHYS* experiment is an increase in the ice water path in the evening (IWP; Figure 7d). This is possibly due to a combination of deeper clouds providing enhanced mass aloft and smaller droplets with lower fall speeds (Fan et al., 2013; Grabowski & Morrison, 2016; Heikenfeld et al., 2019), and potentially CCN-induced convective invigoration (discussed in more detail in following paragraph).

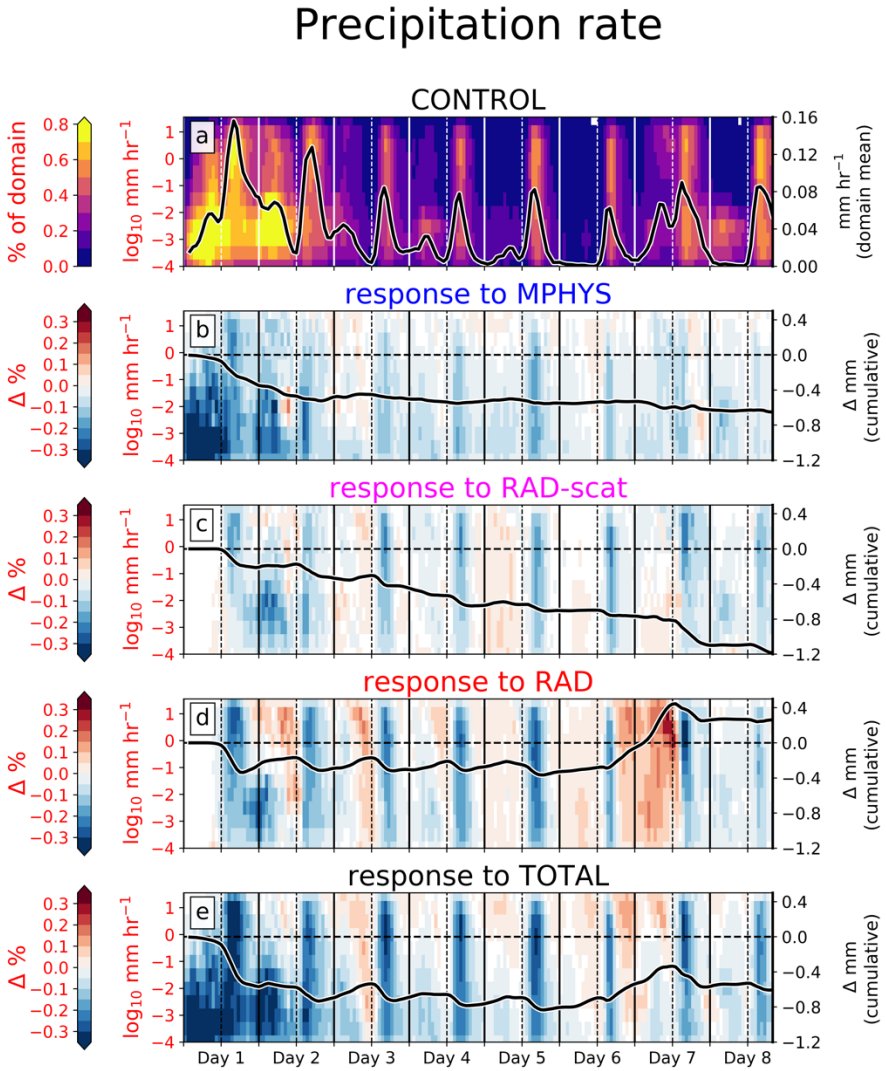

Figure 6. Timeseries of the precipitation intensity occurrence across the domain and response in each experiment. In the control simulation (**a**) the colors depict the percentage occurrence of the domain as a function of precipitation rate (note the $\log_{10}$ scale used for the bins). For all other experiments (**b** – **e**) the colors depict the absolute change in percentage occurrence compared to the control (experiment – control). Panels correspond to responses from: **b** the *MPHYS* experiment; **c** the *RAD-scat* experiment; **d** the *RAD* experiment; and **e** the *TOTAL* experiment. In the control simulations (**a**) the black line shows the domain mean precipitation rate, and in the other experiments (**b** – **e**) the black solid line shows the domain mean cumulative precipitation response (experiment – control); corresponding values are shown on the right-hand-side y-axis in black. Vertical dashed (solid) lines are at 1200 (0000) local solar time for each simulated day.

The domain response to enhanced N_d settles into a consistent diurnal cycle after the first two days. Precipitation is suppressed in weakly precipitating clouds (< 0.01 mm hr^{-1}) throughout much of the simulation and up to rates of 1 mm hr^{-1} during the afternoon convection (Figure 6b). These precipitation rates are insufficient to strongly impact the domain-mean cumulative precipitation which remains at around -0.55 mm from day 3 onwards (Figure 6b). LWP sharply increases during the afternoon convection at 1400 LST (Figure 7c) though this is almost entirely due to increases from clouds with LWP exceeding 1000 g m^{-2}. Similarly, the IWP response (Figure 7d) has a positive peak in the diurnal cycle centered at 1800 LST of ~ +20 g m^{-2} which represents an increase of > 60 %. Due to the slower fall speed of ice particles the peak is

slower to decrease and results in a consistent increase in the IWP throughout the simulation. These results highlight the dominant role that small-scale convective features (representing < 0.5 % of the domain) have on the response of the mean properties of the large-scale environment. Following the initial suppression of w_{max} there is little consistent response in the diurnal cycle (Figure 8b) except at 1400 LST when there is some suppression of weak ($w_{max} \leq 3$ m s^{-1}) updrafts. It is worth noting that updrafts greater than 6 m s^{-1} are generally more prevalent throughout the simulation. This could be attributed to CCN-induced convective invigoration via latent heat released from the additional freezing (Figure 7d); this process would tend to produce a stronger signal in existing cloudy columns with high updraft speeds (and therefore more condensate to freeze), which would support our results, or be a consequence of the overall cloud deepening due to warm-phase invigoration processes. A definite causal attribution would require a more in-depth analysis of the updraft vertical momentum equation that is not attempted here. However, we note that a recent cloud resolving modelling intercomparison study under the umbrella of the Aerosol, Clouds, Precipitation and Climate (ACPC) initiative revealed a dominant contribution of enhanced condensational latent heating of the warm phase of convective clouds, even when saturation adjustment schemes are used, attributable to increased environmental instability in high-CCN conditions.

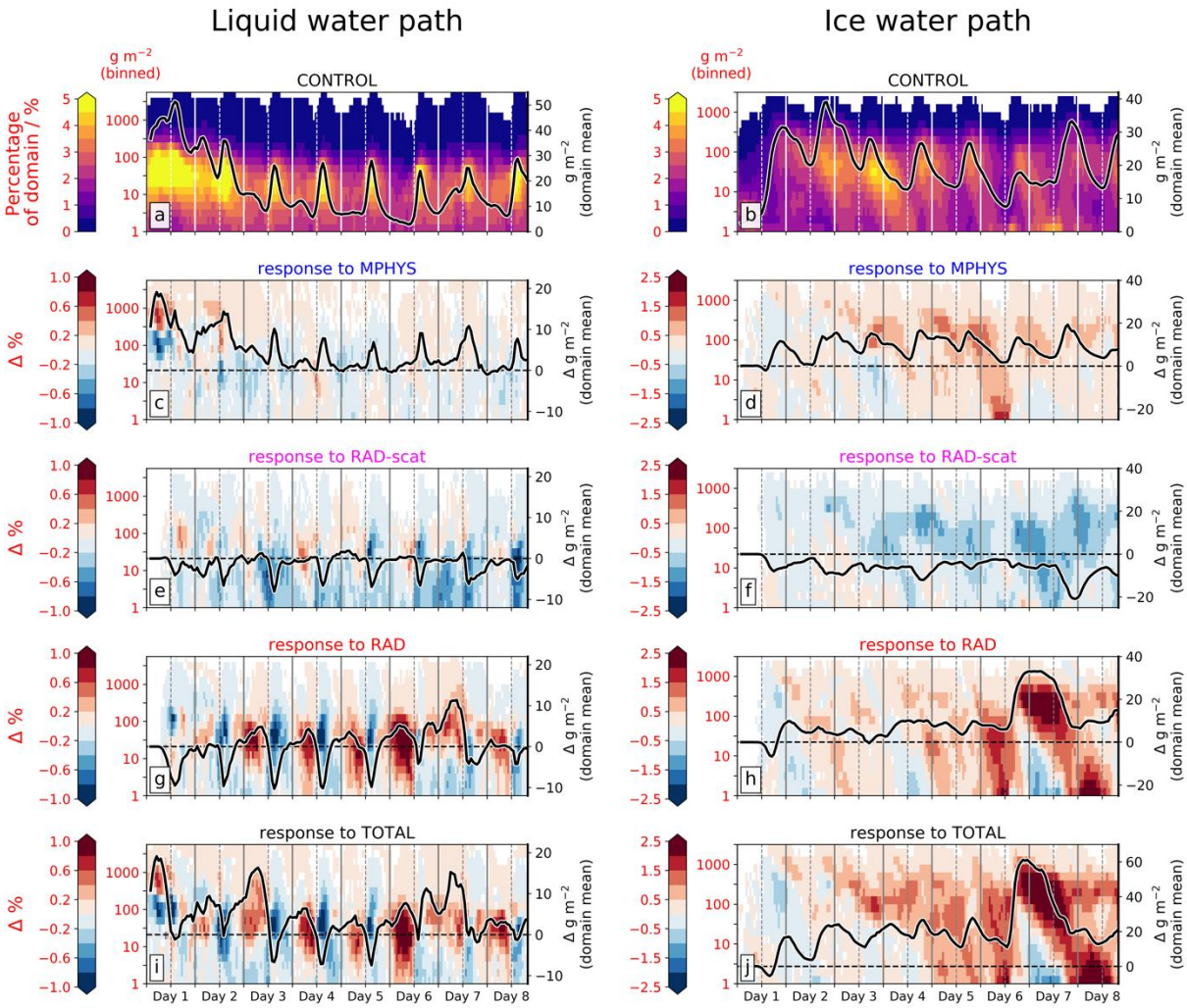

Figure 7. Timeseries of the probability of occurrence of liquid water path (LWP; plots **a**, **c**, **e**, **g**, and **i**) and ice water path (IWP; plots **b**, **d**, **f**, **h**, and **j**) across the domain and the responses in each experiment. In the control simulations (**a** and **b**) the colors depict the percentage occurrence of the domain as a function of LWP and IWP. For all other experiments (**c** – **j**) the colors depict the absolute change in percentage occurrence compared to the control (experiment – control). Panels correspond to responses from: *MPHYS* experiment (**c** and **d**); the *RAD-scat* experiment (**e** and **f**); the *RAD* experiment (**g** and **h**); and *TOTAL* experiment (**i** and **j**). In the control simulations (**a** and **b**) the black line shows the domain mean timeseries, and in the other experiments (**c** – **j**) the black solid line shows the absolute change in the domain mean timeseries (experiment – control); corresponding values are shown on the right-hand side y-axis in black. Vertical dashed (solid) lines are at 1200 (0000) local solar time for each simulated day.

Why do the first two days behave differently? As highlighted, increasing N_d primarily perturbs the cloud properties and has little impact on the large-scale thermodynamic environment. Comparing the precipitation in the control and in the *MPHYS* experiment (Figures 6a and 6b) shows that the marked suppression on days 1 and 2 occurs simultaneously with the high precipitation rates in the control simulation (largely due to spin-up of the model). The same can be seen with the positive LWP response (Figures 7a and 7c). It is only when the perturbation is this strong that we see a response in updraft speeds (Figure 8b). This suggests that the response of the domain to increasing N_d is consistent throughout the simulation, but that the impact is non-linear.

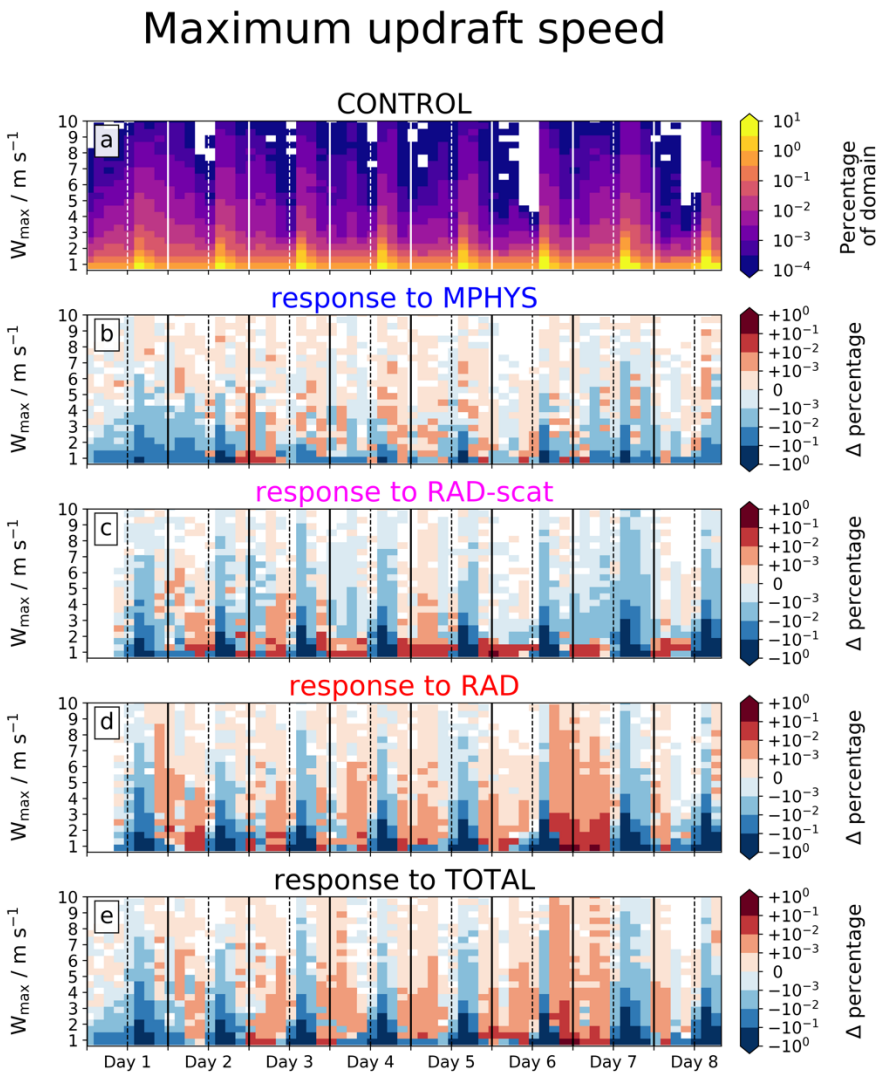

Figure 8. Timeseries of the vertical wind intensity occurrence across the domain and response in each experiment. In the control simulation (**a**) the colors depict the percentage occurrence of the domain grid points as a function of maximum vertical windspeed below 6 km (w_{max}) at each grid point. For all other experiments (**b** – **e**) the colors depict the absolute change in percentage occurrence compared to the control (experiment – control). Panels correspond to responses from: **b** the *MPHYS* experiment; **c** the *RAD-scat* experiment; **d** the *RAD* experiment; and **e** the *TOTAL* experiment. Vertical dashed (solid) lines are at 1200 (0000) local solar time for each simulated day.

3.2.2 *RAD-scat* experiment

The presence of a layer of purely scattering aerosol in the *RAD-scat* experiment (see table 1) strongly reduces downwelling shortwave radiation reaching the surface (~ -50 W m^{-2} domain mean at 1200 LST; not shown) and produces anomalous cooling in the BL of several degrees across the domain (see Figure S1b). Daytime surface fluxes of sensible and latent heat are reduced by ~ 10 % (latter shown in Figure S1d). The cooling strongly suppresses convection during the afternoon and considerably weakens updraft intensities across the domain (Figure 8c) and throughout the simulation. As a result, precipitation decreases during the afternoon (Figure 6c) resulting in a reduction in domain-mean cumulative precipitation by -1.2 mm at the end of the simulation at a rate of almost -0.2 mm day^{-1}. LWP (Figure 7e) similarly decreases in the afternoon and is attributed to clouds with LWP between 100 and 1000 g m^{-2}; along with the pronounced suppression

of w_{max} < 3 m s^{-1} (Figure 8c) this demonstrates that the shallow convective cells with moderate loadings of condensate are predominantly affected by the anomalously cool surface. With weaker updrafts there is a reduction in the amount of condensate reaching the freezing level and an overall decrease in IWP throughout the simulation of ~ -8 g m^{-2}; the IWP response does not have a pronounced diurnal cycle.

The domain-mean low-level (P > 800 hPa) cloud cover (Figure 10e) is generally enhanced by 1 or 2 %, although suppression of afternoon convection often counteracts this and results in a slight diurnal cycle in the response. This helps drive a slight increase in precipitation overnight (Figure 6c) which extends over all precipitation intensities. The cloudiness increases due to an anomalously cooler BL and enhanced moisture in the BL (see Figure S1g), the latter of which occurs due to reduced mixing with the dry FT. An increase in weak updrafts (w_{max} < 3 m s^{-1}; Figure 8c) overnight is likely attributed to this enhanced low-level cloudiness and precipitation. Mid-level (800 to 400 hPa) cloud cover is considerably reduced throughout the simulation, especially at lower cloud fractions (Figure 10f). The daily suppression of convection accounts for the minimum at 1400 LST and is dominated by the decrease of cloud fraction > 0.95; a simultaneous decrease in liquid cloud coverage by ~ 5% across the domain (Figure 9a) suggests these are entire convective cells that have failed to initiate.

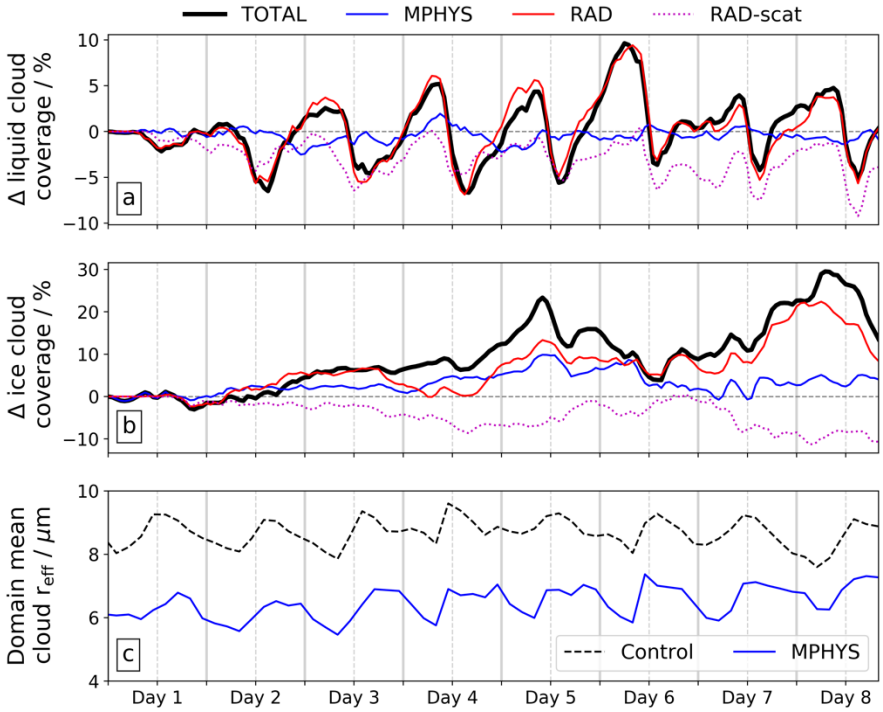

Figure 9. Timeseries showing the change in percentage coverage of the domain with **a** liquid clouds and **b** ice clouds for the experiments compared to the control simulation (experiment – control). Panel **c** shows the domain-mean cloud droplet effective radius for the control simulation and *MPHYS* experiment. Vertical dashed (solid) lines are at 1200 (0000) local solar time for each simulated day.

3.2.3 *RAD* experiment

In the *RAD* experiment the aerosol layer not only reduces the downwelling shortwave at the surface (as with *RAD-scat*) but also produces a localized source of heating during the day throughout the BL (see Figure 3a for the aerosol profile). The primary role that this heating aloft has on the domain is to enhance cloudiness, precipitation, and convective activity overnight and increase the magnitude of the response during the day.

The suppression of afternoon convection from the anomalously cool BL is further enhanced by the heating aloft, which acts to stabilize the BL (Figure 8d); precipitation in the afternoon is also further decreased at all intensities (Figure 6d) especially at rates ≥ 1 mm hr^{-1}, as is the LWP which reaches a domain mean of -10 g m^{-2} at 1400 LST on most days of the simulation. During the afternoon the anomalous heat aloft is mixed throughout the BL and increases CAPE (see Figure S1f); convective activity from the organized mesoscale cells is enhanced overnight (Figure 8d), increasing LWP (Figure 7g) and precipitation (Figure 6d) up until midday. The enhanced precipitation overnight counteracts the daytime suppression, preventing the gradual anomalous decrease in cumulative precipitation as observed in the *RAD-scat* experiment. The enhanced

convective activity overnight increases IWP at high loadings (Figure 7h), which gradually spreads to lower values throughout the following 24 hours (note the diagonal features), and produces an overall increase in IWP and high-altitude cloud coverage (Figure 9b) throughout the simulation.

In the *RAD-scat* experiment anomalous BL cooling enhanced low-level clouds throughout the simulation. The addition of heating aloft prevents this via a partial offset in the BL cooling (Figure S1b) and evaporation of cloud, resulting in suppression of low-level cloud in the afternoon (Figure 10g). As the simulation progresses the low-level cloud cover displays a positive trend on top of the afternoon suppression. This is driven by a steady increase in the water vapor content (Q_{vapor}) in the BL (see Figure S1h) that reaches a domain mean value of +0.75 g kg^{-1} (~ +7 %); this is partially driven by suppressed mixing with the FT but also anomalous convergence centered beneath the BBA plume (Figure 11d). The gradual increase in Q_{vapor} also enhances CAPE (see Figure S1f) but primarily in the region of anomalous convergence beneath the plume. Mid-cloud cover response (Figure 10h) is primarily driven by the afternoon suppression of convection but occasional small positive anomalies overnight demonstrate an impact from the enhanced activity overnight, similar to the LWP response.

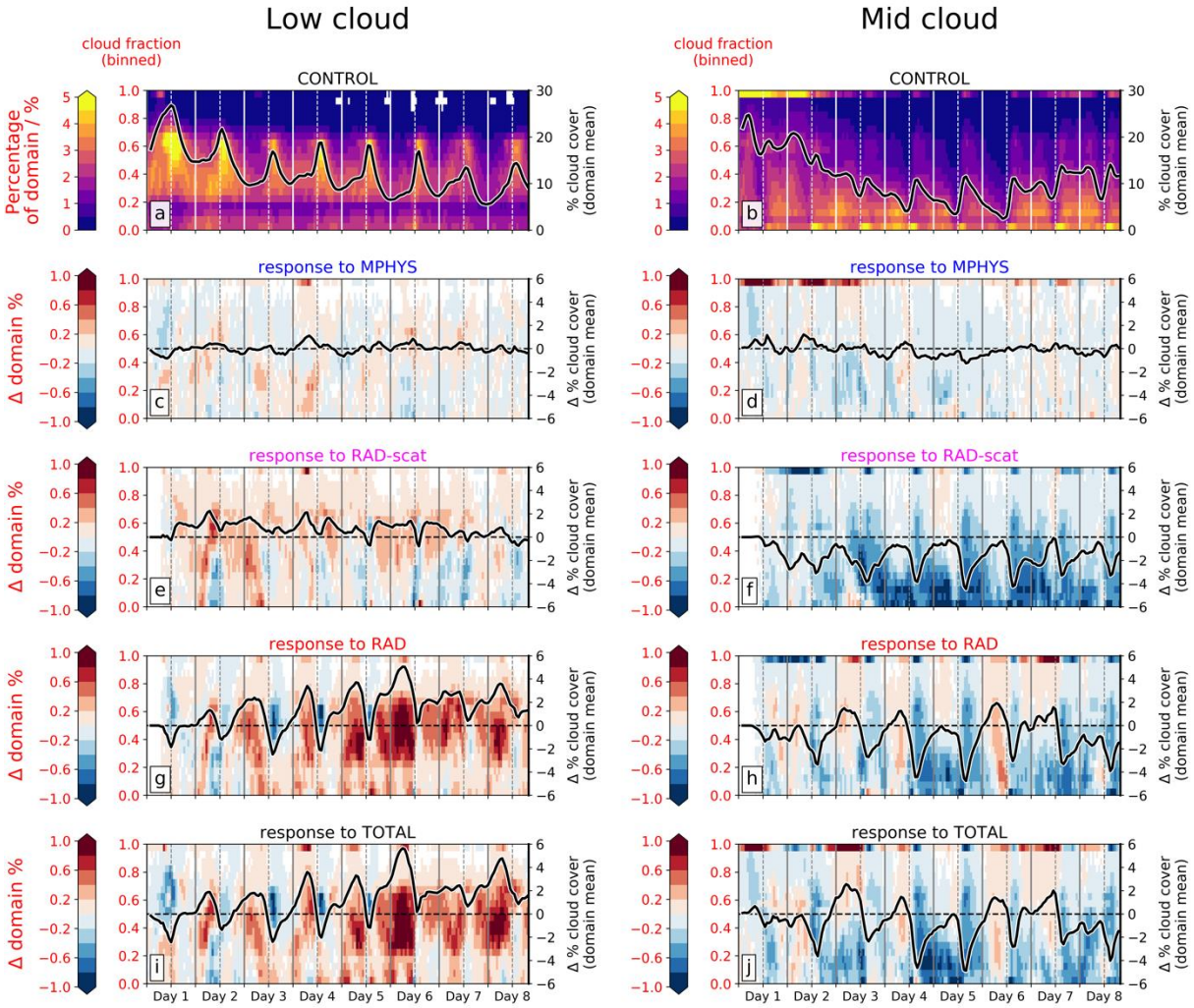

Figure 10. Timeseries of the probability of occurrence of low cloud fraction (plots **a**, **c**, **e**, **g**, and **i**) and mid cloud fraction (plots **b**, **d**, **f**, **h**, and **j**) across the domain and the responses in each experiment. In the control simulations (**a** and **b**) the colors depict the percentage occurrence of the domain as a function of cloud fraction. For all other experiments (**c** – **j**) the colors depict the absolute change in percentage occurrence compared to the control (experiment – control). Panels correspond to responses from: *MPHYS* experiment (**c** and **d**); the *RAD-scat* experiment (**e** and **f**); the *RAD* experiment (**g** and **h**); and the *TOTAL* experiment (**i** and **j**). In the control simulations (**a** and **b**) the black line shows the domain mean timeseries of percentage cloud cover, and in the other experiments (**c** – **j**) the black solid line shows the absolute change in the domain mean percentage cloud cover (experiment – control); corresponding values are shown on the right-hand side y-axis in black. Vertical dashed (solid) lines are at 1200 (0000) local solar time for each simulated day.

Overnight on day 6/7 there is a considerable anomalous increase in precipitation (Figure 6d) and IWP (Figure 7h), with an associated increase in updraft speeds (Figure 8d). This corresponds to the intensification of a mesoscale convective cell in the west of domain, downwind of the plume center. The cell, present in the control simulation, becomes larger and deeper and produces widespread intense precipitation and produces extensive convective outflow that persists for ~36 hours (Figure 7h). Figure S2 in the supporting information provides a snapshot of the feature at 0500 LST on day 7.

3.2.4 *TOTAL* experiment

In this experiment the full effect of the BBA is examined. We find that the two effects (microphysical and radiative) largely act independently, with the resulting total response approximating a combined effect. Having said that, the radiative effect is dominant and controls much of the mean response over the domain and in some instances the microphysical effects buffer the radiative effects. The response of updraft intensities (Figure 8e) and large-scale circulation (Figure 11e) is almost entirely driven by the radiative effects except for the initial hours before sunrise on day 1. With minimal impact on cloud cover seen in the *MPHYS* experiment (Figures 10c and 10d) it follows that the total response of low and mid-cloud cover is controlled by the radiative effect (Figures 10i and 10j), which is illustrated by overlapping timeseries for the response in cloud-free fraction in the *RAD* and *TOTAL* experiments (Figure 9a).

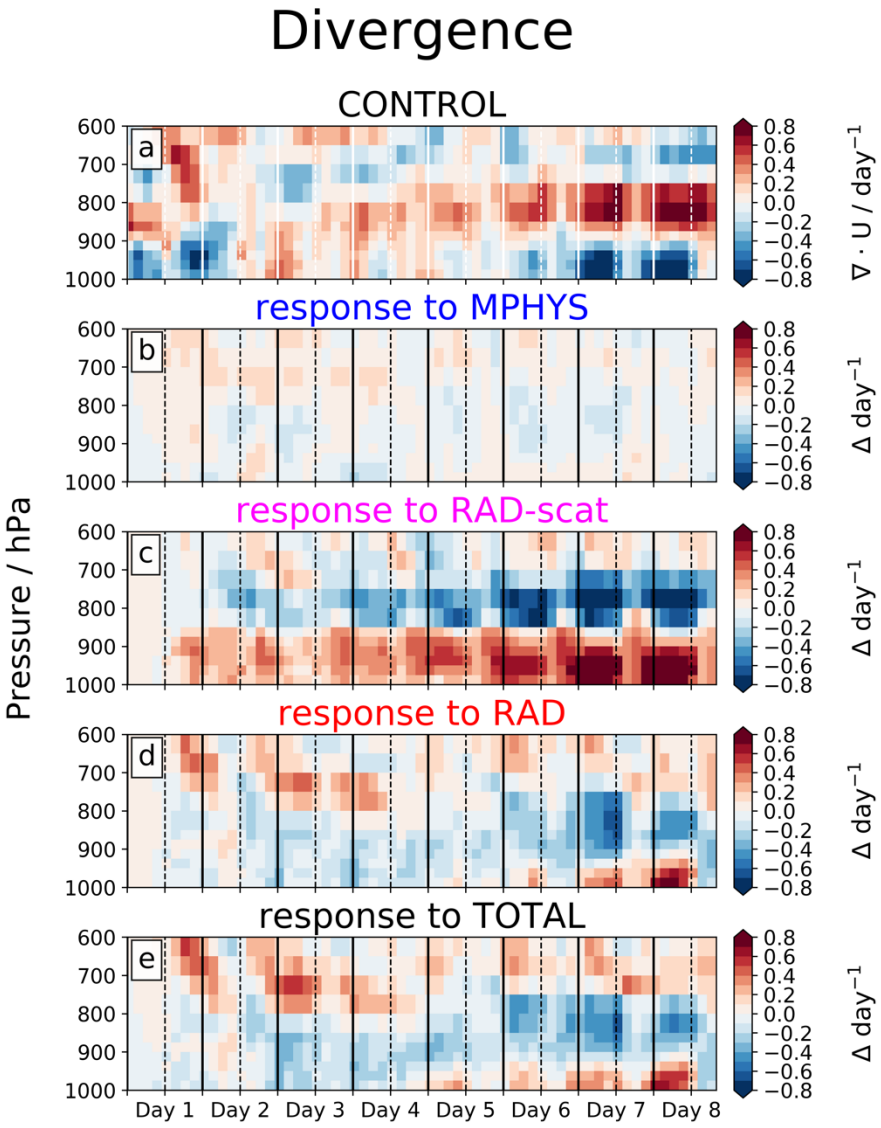

Figure 11. Timeseries showing the regional mean profile of horizontal divergence in the control simulation (**a**) and the absolute change in the experiments (**b** – **e**) compared to the control (experiment – control) in the southwest corner of the domain where the AOD perturbation is the greatest (67 to 59°W, 14 to 6°S). Positive values in **b** – **e** represent anomalous divergence of air, and negative values represent anomalous convergence. Vertical dashed (solid) lines are at 1200 (0000) local solar time for each simulated day.

Cloud formation and development is impacted by radiative effects, and cloud properties are directly impacted by changes to N_d. This is reflected in the LWP, IWP, and precipitation responses (Figures 7i, 7j, and 6e) that demonstrate a combined effect from both microphysics and radiation. The diurnal cycle from the *RAD* precipitation response is still apparent (Figure 6e), but has become offset by an overall suppression by the enhanced N_d, resulting in a more pronounced decrease in domain-mean cumulative precipitation which decreases by -0.6 mm on the first day and then remains roughly at this value for much of the simulation. The precipitation histogram highlights that radiative effects primarily impact the higher rates (> 1 mm hr^{-1}) from convective cells, whilst microphysical effects are more apparent at lower rates (< 1 mm hr^{-1}) associated with shallower convection and stratiform cloud. However, the two effects are not entirely independent: a suppression of the highest precipitation rates overnight (comparing *RAD* with *TOTAL* experiment) are caused by the enhanced N_d, which acts to dampen the response. This is most evident overnight on day 6/7 as the intensification of the mesoscale convective cell is weakened.

The response of the LWP is a combination of both radiative and microphysics effects. During afternoon convection at 1400 LST the two effects have opposite responses of equal magnitudes, yet the total effect is dominated by the radiative effect. A suppression of convection results in fewer and less intense convective cells, which are *then* impacted by the enhanced N_d, hence why the response in the *TOTAL* experiment is more aligned to the *RAD* experiment. The IWP response (Figures 7j and 9b) is closely aligned with an additive effect from both radiative and microphysical effects, resulting in a large increase in domain-mean IWP and ice-cloud coverage throughout much of the simulation that often doubles the IWP in the control simulation. The linearity of the LWP and IWP responses from *RAD* and *MPHYS* are shown in Figure S3.

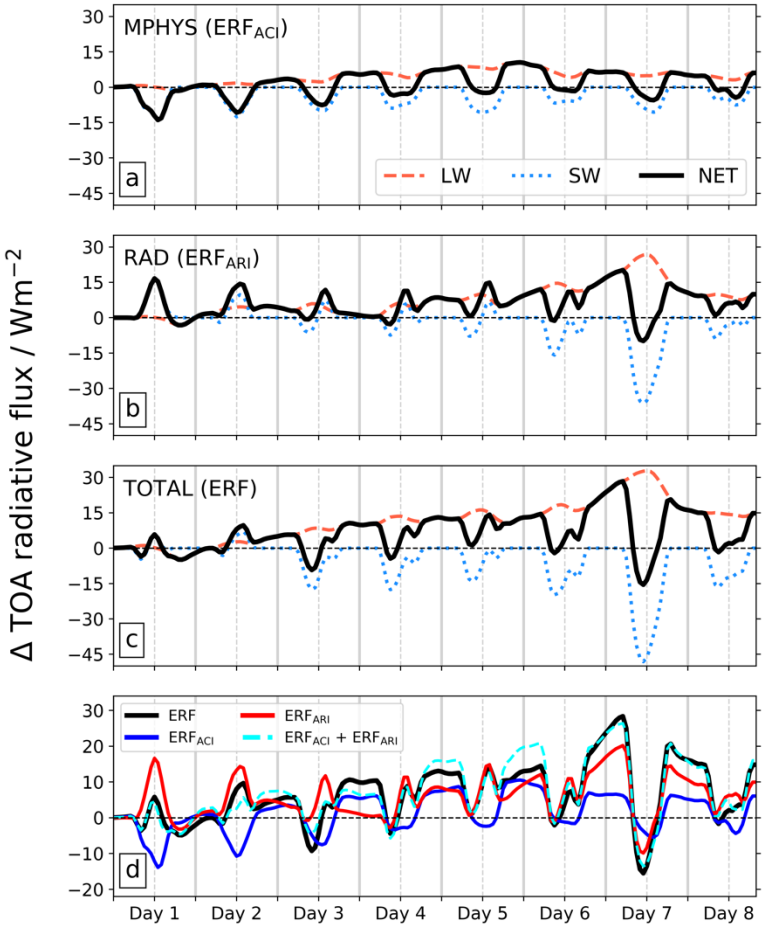

Figure 12. Timeseries showing the domain-mean TOA effective radiative forcing (ERF) in the *MPHYS* (**a**; ERF_{ACI}), *RAD* (**b**; ERF_{ARI}), and *TOTAL* (**c**; ERF) experiments. Blue dotted lines show the SW component, red dashed lines show the LW component, and solid back lines show the NET (SW + LW) response. The NET component from each experiment in **a**, **b** and **c** are individually re-plotted in **d** and show the ERF_{ACI} (blue line), ERF_{ARI} (red line), ERF (black line), and ERF_{ACI}+ERF_{ARI} (cyan dashed line). Note the change in scale on the y-axis for plot **d**. Negative values represent a cooling effect and vice versa. Vertical dashed (solid) lines are at 1200 (0000) local solar time for each simulated day.

3.3 Top-of-atmosphere radiative effects

Figure 12 shows the domain-mean top-of-atmosphere (TOA) effect on radiation due to the presence of the BBA. Values from the *MPHYS*, *RAD*, and *TOTAL* experiments are shown for shortwave (SW), longwave (LW), and net (NET; SW + LW) components, with negative values representing a cooling effect on the climate.

In the *MPHYS* experiment the SW_{TOA} response is consistently negative, reaching a maximum magnitude of ~ -15 Wm^{-2} at 1200 LST on most days. There is little change in the low and mid-cloud cover (Figures 10c and 10d) and the sharp increase in domain-mean LWP (Figure 7c) is attributed to clouds with high loadings of water that already have a high albedo, demonstrating the response is primarily driven by a large-scale reduction in cloud droplet effective radius (Figure 9c) that increases the albedo of clouds with moderate loadings of water. In the *RAD* experiment the SW_{TOA} response shows considerable temporal variation. Initially the response is positive with a magnitude of ~ +15 W m^{-2} but a diurnal response develops and evolves into a consistent negative response. These responses are a combination of the positive direct effect from the BBA absorption and the temporally varying low-cloud response (Figure 10g). In both *MPHYS* and *RAD* experiments the LW_{TOA} response is positive throughout the simulation due to enhanced IWP. The sharp diurnal cycle in IWP response for the *MPHYS* experiment (Figure 7d) is not duplicated in the LW_{TOA} response (Figure 12a); as with the SW_{TOA} this suggests that the LW_{TOA} response is most sensitive to the clouds that have relatively moderate loadings of ice. This is in contrast to the *RAD* experiment which shows the LW_{TOA} response is closely aligned to the IWP response (Figure 7h); this occurs because the cloud field itself is being perturbed, with more convective activity overnight that results in more high-altitude cloud coverage (Figure 9b).

Table 2. Daily mean BBA effective radiative forcing (ERF) from the TOTAL experiment for LW, SW, and NET components. All values are for the domain-mean ERF (experiment – control) in W m^{-2}.

ERF	Day 1	Day 2	Day 3	Day 4	Day 5	Day 6	Day 7	Day 8
Longwave	-1.0	1.8	7.8	11.8	13.2	16.7	26.6	14.7
Shortwave	0.1	1.0	-4.5	-4.5	-3.4	-6.4	-15.9	-6.5
Net	-1.0	2.8	3.3	7.3	9.8	10.3	10.6	8.2

The NET_{TOA} response for each experiment, also referred to as effective radiative forcing (ERF), is shown in Figure 12d and daily mean values presented in Table 2. The ERF (determined from the *TOTAL* experiment) has contributions from ERF_{ACI} (determined from the *MPHYS* experiment) and ERF_{ARI} (determined from the *RAD* experiment). The initial response is characterized by strong opposing SW effects from ERF_{ARI} and ERF_{ACI} (Figure 12c), resulting in an overall weak ($\leq$ 1 Wm^{-2}) and positive daily mean ERF. As the simulation progresses the daily mean ERF becomes increasingly positive due to an increasing LW component, driven by enhanced ice, which results in a positive ERF_{ARI} and ERF_{ACI}. A positive ERF_{ACI} due to the ice phase response was also reported by Dagan et al. (2020). By day 5 the ERF is close to 10 W m^{-2}, driven predominantly by a strong LW component of 13 W m^{-2}.

These results demonstrate two important findings. First, the response of IWP and high-altitude cloud cover to BBA plays a significant role in determining its overall ERF: if the IWP response is weaker, as reported by Liu et al. (2020) and discussed later, then the ERF is instead controlled by perturbations to the liquid cloud field and has an opposite sign, i.e., a cooling rather than warming effect on climate. Second, the ERF from BBA is highly time-dependent: all TOA radiative effects (LW, SW, and NET) are initially weak but then tend to grow in magnitude throughout the simulation, and are therefore highly sensitive to the longevity and horizontal coverage of the BBA plume.

3.4 AOD-dependence

The results so far have demonstrated that the response of the domain to the BBA is highly complex and dependent on the longevity of the plume, which makes the representation of its effects in coarser models difficult. Here we identify a relationship between the BBA perturbation (ΔAOD) and the suppression of afternoon convection, a key driver of BBA impacts in our simulations.

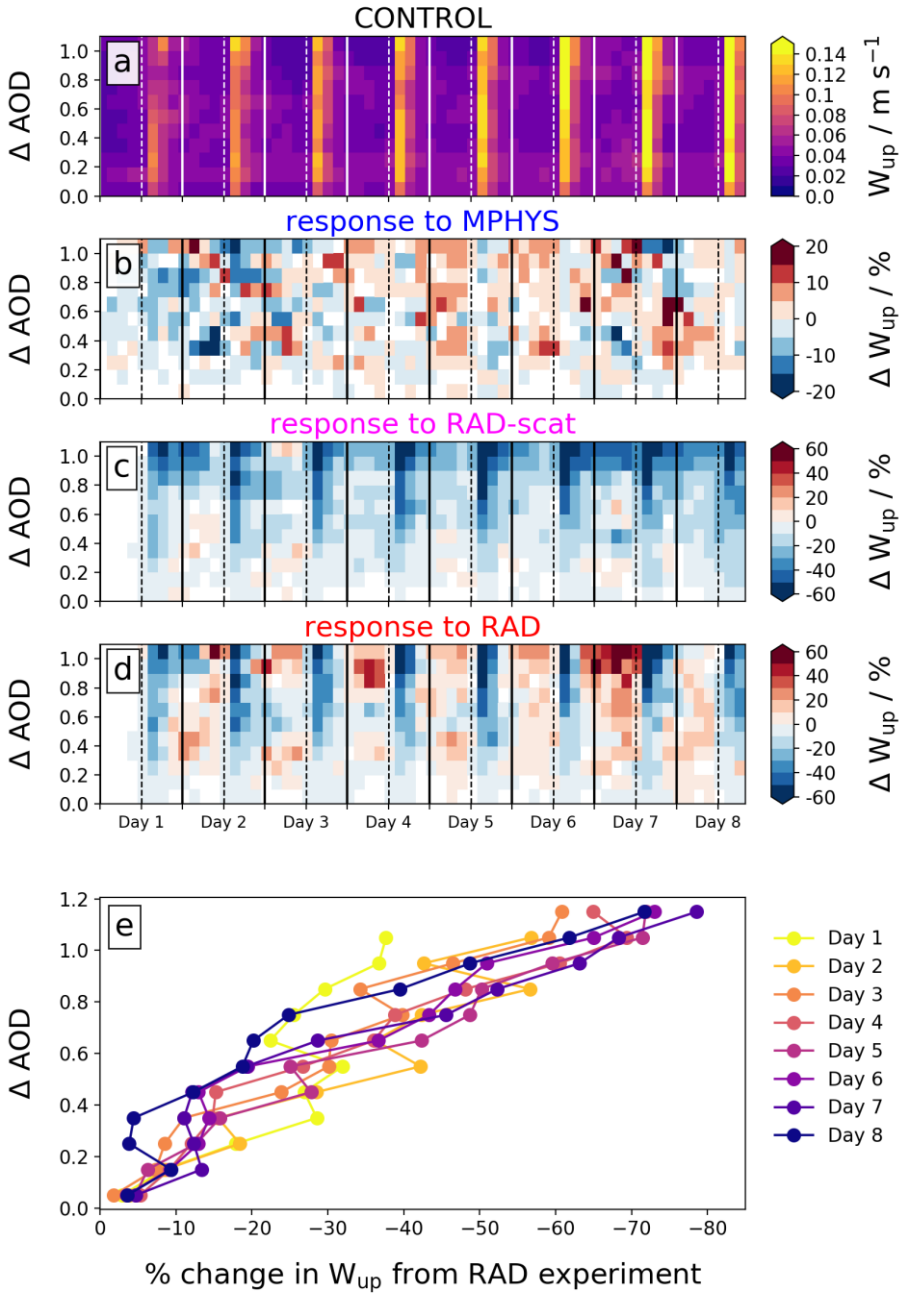

Figure 13. Timeseries showing the probability of occurrence of mean updraft speed (w_{up}; calculated between the surface and 700 hPa) as a function of mean ΔAOD (**a** – **d**). Colors in the control simulation (**a**) depict the absolute value of w_{up} whereas in the *MPHYS* (**b**), *RAD-scat* (**c**) and *RAD* (**d**) experiments the colors show the percentage change compared to the control (experiment – control). Note the different color scale used in **b**. Vertical dashed (solid) lines are at 1200 (0000) local solar time for each simulated day. Plot **e** shows the percentage change in mean w_{up} as a function of mean ΔAOD in the *RAD* experiment at 1400 local solar time on each day of the simulation (depicted as different colors); data is taken from plot **d**.

In Figure 13 we use the prescribed horizontal distribution of AOD provided by the plume model (Figure 3b) to subset the column-mean updraft speed between the surface and 700 hPa (w_{up}) and its response in the *RAD* and *RAD-scat* experiments. Data is downscaled to a resolution of 0.5 degrees and mean values for each subset of pixels, stratified by ΔAOD, determined at each output timestep. Figure 13a shows the distribution

of w_{up} as a function of ΔAOD in the control simulation. The daily afternoon convection is visible at 1400 LST at all ΔAOD values, demonstrating that the highest updraft speeds are dispersed around the domain, rather than co-located with the simulated BBA plume. The *MPHYS* experiment response (Figure 13b) shows no evidence of a consistent impact to w_{up} nor a clear dependence on ΔAOD, which supports our earlier hypothesis that there is no widespread CCN-induced cloud invigoration occurring in these simulations. The response of w_{up} in the *RAD-scat* experiment (Figure 13c) clearly demonstrates an overall suppression throughout the simulation up to a value of -60 % during the periods of afternoon convection. There is also evidence of a relationship between ΔAOD and w_{up}, with greater AOD perturbations occurring alongside a greater suppression of w_{up}. This is mostly evident at 1400 LST when the strongest updrafts occur (Figure 13a). Including the in-situ heating in the *RAD* experiment (Figure 13d) enhances convective activity overnight but does not display a consistent dependence on ΔAOD. Importantly, the addition of heating does not impact the suppression of convection at 1400 LST.

The convection that occurs at 1400 LST produces the greatest values of LWP, IWP, and precipitation during the diurnal cycle, therefore we focus on this time period in Figure 13e. This data is taken directly from Figure 13d (for the *RAD* experiment) and plotted individually for each day of the simulation. The data provide more evidence of a relationship between the plume ΔAOD and the suppression of convection. At values of ΔAOD = 0.2 there is a suppression of mean updraft speeds by roughly 10 %, and at ΔAOD = 0.8 the suppression has increased to roughly 40 %. There is some day-to-day variability but all data tends towards a similar relationship. The resulting relationship is likely driven by the formation of fewer convective cells and a weakening of existing cells, a hypothesis that requires further work to test.

This result provides a quantitative means to relate the large-scale suppression of convection to AOD from BBA smoke, and additionally shows that this relationship is caused by the anomalous surface cooling that occurs due to the extinction of shortwave radiation by the aerosol and is therefore applicable to other aerosol species such as dust or smoke with higher SSA values. Figure 13c also demonstrates that the intensification of convection due to the heating aloft is not clearly dependent on ΔAOD, though there are signs of intensification during the night at higher values of ΔAOD.

4 Discussion and conclusions

In this study we used the ICON model in a regional configuration to study the impact of BBA smoke plumes on clouds and precipitation processes over the Amazon rainforest, with a domain covering 3000 x 2000 km at a resolution of 1500 m that allows us to resolve the convective processes that drive the diurnal cycle over the region. The MACv2-SP model (Stevens et al., 2017) was used to simulate a BBA plume with a horizontal and vertical distribution consistent with observations, and a realistic N_d distribution was produced using an observationally informed relationship between AOD and N_d. A series of experiments were designed to isolate the different pathways through which the BBA plume influences the atmosphere in the domain: 1. enhanced CCN and N_d (isolating ACI); 2. reduction in surface downwelling radiation (isolating surface cooling); 3. surface cooling and in-situ heating of BBA (isolating ARI); and 4. the total effect of simultaneously enhanced N_d, surface cooling, and in-situ heating (ARI and ACI).

Our main findings are as follows:

- ACI primarily perturbs the intensive cloud properties with evidence of cloud deepening, whereas ARI influences formation and development of convective cells and the convergence of moisture.
- ARI strongly suppresses convective activity (mean updrafts in the lower troposphere) in the afternoon primarily due to anomalous surface cooling; heating aloft further stabilizes the BL and enhances the suppression in the afternoon though promotes the intensification of organized convection overnight.
    - A potential relationship between the smoke AOD perturbation and the percentage response of the mean updraft speed during the afternoon was presented. In these simulations a smoke AOD of 0.5 weakens the mean updraft speed in the troposphere by ~ 25 %, and an AOD of 1.0 by ~ 65 %.
- Suppressed convection during the daytime weakens mixing between the BL and FT, enhancing low-level moisture; heating aloft induces anomalous convergence beneath the plume, further enhancing

low-level moisture. This also implies that the 10 % reduction in surface latent heat flux is of secondary importance.

- ARI predominantly impacts high precipitation rates (> 1 mm hr^{-1}); surface cooling drives reduction in convective precipitation, whereas heating aloft enhances precipitation during the night. ACI predominantly impacts low-to-moderate precipitation rates (< 1 mm hr^{-1}) through a weakening of the warm rain process.
- Domain-mean impacts from ACI on LWP and IWP are biased towards deep convective clouds with high loadings of condensate.
- ARI strongly impacts the coverage of liquid and ice clouds: liquid cloud cover decreases during daytime by -5 % and increases overnight by +5%; ice cloud cover gradually increases though not consistently.
- Both ACI and ARI result in enhanced IWP. ARI-induced intensification of cells overnight transports more condensate to freezing level, enhancing IWP and horizontal extent, whilst ACI-induced reduction in cloud droplet size results in more IWP from existing deep convective clouds. There was no evidence of significant CCN-induced cloud-invigoration from ACI.
- TOA radiative effects are complex and show considerable sensitivity to the BBA plume longevity.
    - The TOA shortwave effect from ARI is a combination of the positive direct effect from BBA absorption and the response of the low-level cloud driven by three mechanisms: BL cooling (thicker clouds); cloud-burn off (suppressed clouds during daytime); and an overall moistening of the BL (gradual offset to enhanced cloudiness).
    - The TOA shortwave effect from ACI is consistently negative and driven primarily by a reduction in the cloud droplet effective radius from clouds with moderate loadings of liquid.
    - Enhanced IWP throughout simulation drives a positive TOA longwave effect that grows in magnitude, attributed to both ARI and ACI.
    - The daily mean net TOA radiative effect is dominated by the LW effect and although starting slightly negative (-1 W m^{-2} on day 1) becomes increasingly positive (+3.5 W m^{-2} on day 3, +10 W m^{-2} by day 6).

Our results largely support the findings in previous modelling studies though there are some differences that highlight the importance of resolving convective processes and the response of the IWP. The primary impact of BBA on the domain is a suppression of convection beneath plume, which is consistent with previous studies (Liu et al., 2020; Martins et al., 2009; Wu et al., 2011). Other modelling studies have reported an overall decrease in cumulative precipitation due to smoke presence (Liu et al., 2020; Martins et al., 2009; Thornhill et al., 2018; Wu et al., 2011) but the possibility of increased peak intensities (Martins et al., 2009). These results agree with our study: the suppression of convection (ARI) and the warm-rain process (ACI) both contribute to suppressed precipitation during the afternoon; however, we observed an increase in precipitation overnight that partially counteracted the daytime suppression; we also observed the intensification of a mesoscale convective cell towards the end of the simulation. Birch et al. (2014) have shown that the diurnal cycle of convection and associated precipitation over West Africa is not well represented by coarse-resolution models that parameterize convection; therefore, the diurnal response of convection that we observe would not be reproduced by climate models. An analysis of precipitation over the Amazon region in CMIP5 models shows a dry model bias throughout the dry season (Yin et al., 2013); it is possible that this is driven by a poorly represented diurnal cycle of convection. A replication of our simulations using a coarser resolution and parameterized convection would allow us to understand whether key responses to smoke are reproduced in this region, and bridge the gap between regional- and global-scale models.

Our simulations provide evidence that large-scale impacts on circulation and moisture transport are driven by perturbations to the radiation, rather than N_d. Surface cooling promotes anomalous divergence, whereas heating aloft promotes anomalous convergence, with the latter dominating. Lee et al. (2014) also reported the two processes often result in opposing impacts on the circulation. Hodzic & Duvel (2018) studied the impact of BBA over the forested island of Borneo and found that moderately absorbing BBA induced anomalous divergence, whereas strongly absorbing BBA induced anomalous convergence; as in our study, this indicates a competition between the surface cooling effect and heating aloft driven by radiation. In contrast to our results, Zhang et al. (2008) found anomalous moisture divergence below the smoke region

due to surface cooling, despite the heating aloft. This may be attributed to a coarser resolution (60 km) and differences in the representation of convective processes: along with enhanced stability during the daytime we also observed enhanced CAPE aloft and intensification of turbulence overnight which was not reported by Zhang et al. (2008). Enhanced CAPE aloft and invigorated updrafts were reported by Wu et al. (2011); our results support this hypothesis and show that this is an important response in the diurnal response of precipitation.

A recent study by Liu et al. (2020) provides a good comparison to our study. Using 7-day WRF-Chem simulations at convection-permitting resolution (3 km) the authors isolated the impacts of smoke on the Amazon to ARI and ACI. Focusing on the final day of the simulation, they found that ARI suppressed low-level clouds due to cloud burn-off and enhanced updrafts aloft, thus increasing IWP; we observed a similar response but additionally saw an overall moistening of the BL which offset the low-level cloud suppression. The authors found that ACI enhanced low-level clouds and suppressed updrafts and IWP; in our study the IWP was enhanced despite a weak suppression of updrafts. We observe pronounced increases (often exceeding 20 g m^{-2}) in IWP due to both ARI and ACI (Figure 7), whereas Liu et al. (2020) observed perturbations below 0.5 g m^{-2}. This discrepancy in IWP response between models could be attributed to previously reported underestimations in WRF (Baró et al., 2018) which are illustrated by the poor agreement between model and observations in Liu et al. (2020). Given that the IWP response in our simulations drives a strong positive LW_{TOA} radiative effect this highlights an important sensitivity of the simulated response of the Amazon rainforest to smoke.

Our simulations are supported by observations from in-situ and space-borne observations, and additionally highlight the importance of observing the full diurnal cycle for quantifying the overall impact of smoke on the Amazon. In-situ observations point towards smoke generally suppressing precipitation during the dry season (Andreae et al., 2004; Bevan et al., 2008; Camponogara et al., 2014; Gonçalves et al., 2015) alongside convective invigoration within unstable atmospheres (Gonçalves et al., 2015) and existing updrafts (Andreae et al., 2004). We observed an overall suppression of precipitation, though we occasionally observed an intensification of convection in the evening and overnight. Space-borne observations show a relationship between high AOD and the suppression of convection (Jiang et al., 2018; Kaufman & Nakajima, 1993) alongside a suppression of low-cloud cover (Koren et al., 2008) and cloud optical depth (Ten Hoeve et al., 2012). These observations were made with instruments within the A-train satellite constellation which has a local overpass time of ~ 1330 LST. During this time frame the results from our simulations are consistent with these observations. However, our simulations suggest there are strong diurnal responses in LWP, IWP, cloud cover, convection, and precipitation, that cannot be observed by polar orbiting satellites such as those used in the aforementioned studies. The use of geostationary satellites would be ideal for assessing the conclusions of our study.

Yu et al. (2007) used satellite observations (local overpass of ~1330 LST) during two years with contrasting meteorological conditions. The authors found that large-scale cloud fraction decreased with AOD in the drier and more-stable year, but increased for the moister, more unstable year; our simulations may help understand how such a dichotomy could be achieved. In a ‘stable’ year the suppression of convection is less effective, which would result in cloud-burn off being a prominent impact from ARI, and resulting in decreased cloud cover. In a more ‘unstable’ year the suppression of convection is more active and sets up anomalous convergence below the smoke plume and reduces mixing of drier FT air into the BL. In our simulations this gradually enhanced moisture content in the BL and enhanced low-cloud cover. Although difficult to evaluate this does offer a possible explanation for the contrasting response.

A novel aspect of our study was isolating the surface cooling effect and the heating aloft. Although primarily used to understand the different processes, it also allows us to estimate the impact of the increasing single-scattering albedo that accompanies the recently observed shift of burning from forests to grassland (Ten Hoeve et al., 2012). Higher values of SSA result in the same extinction but reduce the absorption of solar radiation, and relatively enhance the role of surface cooling. Our simulations suggest that this would weaken the intensification of convection overnight, drive a stronger suppression in precipitation, and reduce cloud cover.

By presenting the full 8-day timeseries of the domain response to smoke we are able to consider the role of smoke plume lifetime. Figure 2 demonstrates that there is considerable variation in the duration of time that smoke plumes are present over a single location. In our simulations the response of low-cloud cover was driven by a gradual moistening of the BL, resulting in contrasting SW_{TOA} radiative effects at the beginning and end of the simulation. The gradual increase in IWP throughout the simulation similarly drove contrasting LW_{TOA} radiative effects. Table 2 highlights the consequences of this: the daily mean NET_{TOA} radiative effect is -1 W m^{-2} on day 1 and +10 W m^{-2} by day 6, which suggests that short-lived smoke plumes have a weaker impact on the climate than long-lived smoke plumes. This conclusion also holds true if we neglect the IWP response and instead focus on the SW_{TOA} radiative response that is driven by the low-cloud response.

Acknowledgements

This research was supported by the European Research Council (ERC) project constRaining the EffeCts of Aerosols on Precipitation (RECAP) under the European Union's Horizon 2020 research and innovation programme with grant agreement no. 724602 and from the European Union's Horizon 2020 research and innovation programme project Constrained aerosol forcing for improved climate projections (FORCeS) under grant agreement No 821205. The simulations were performed using the ARCHER UK National Supercomputing Service. IMERG data was obtained via the NASA Goddard Earth Sciences Data and Information Services Center (https://gpm1.gesdisc.eosdis.nasa.gov/data/GPM_L3/GPM_3IMERGHH.06). ERA-Interim and ERA-5 datasets provided by ECMWF were obtained via the MARS client and are available online (https://apps.ecmwf.int/datasets/). AERONET data is available online (https://aeronet.gsfc.nasa.gov). Data and scripts for generating figures from this manuscript can be found at http://doi.org/10.5281/zenodo.4445780. Please contact the authors for access to the full dataset.

References

Albrecht, B. A. (1989). Aerosols, cloud microphysics, and fractional cloudiness. *Science*, *245*(4923), 1227–1230. https://doi.org/10.1126/science.245.4923.1227

Andreae, M. O., Rosenfeld, D., Artaxo, P., Costa, A. A., Frank, G. P., Longo, K. M., & Silva-Dias, M. A. F. (2004). Smoking Rain Clouds over the Amazon. *Science*, *303*(5662), 1337–1342. https://doi.org/10.1126/science.1092779

Aragão, L. E. O. C., Malhi, Y., Roman-Cuesta, R. M., Saatchi, S., Anderson, L. O., & Shimabukuro, Y. E. (2007). Spatial patterns and fire response of recent Amazonian droughts. *Geophysical Research Letters*, *34*(7). https://doi.org/10.1029/2006GL028946

Baró, R., Jiménez-Guerrero, P., Stengel, M., Brunner, D., Curci, G., Forkel, R., et al. (2018). Evaluating cloud properties in an ensemble of regional online coupled models against satellite observations. *Atmospheric Chemistry and Physics*, *18*(20), 15183–15199. https://doi.org/10.5194/acp-18-15183-2018

Bevan, S. L., North, P. R. J., Grey, W. M. F., Los, S. O., & Plummer, S. E. (2008). The impact of atmospheric aerosol from biomass burning on Amazon dry-season drought. In *European Space Agency, (Special Publication) ESA SP* (Vol. 114). John Wiley & Sons, Ltd. https://doi.org/10.1029/2008jd011112

Birch, C. E., Parker, D. J., Marsham, J. H., Copsey, D., & Garcia-Carreras, L. (2014). A seamless assessment of the role of convection in the water cycle of the West African Monsoon. *Journal of Geophysical Research: Atmospheres*, *119*(6), 2890–2912. https://doi.org/10.1002/2013JD020887

Boisier, J. P., Ciais, P., Ducharne, A., & Guimberteau, M. (2015). Projected strengthening of Amazonian dry season by constrained climate model simulations. *Nature Climate Change*, *5*(7), 656–660. https://doi.org/10.1038/nclimate2658

Bond, T. C., Doherty, S. J., Fahey, D. W., Forster, P. M., Berntsen, T., DeAngelo, B. J., et al. (2013). Bounding the role of black carbon in the climate system: A scientific assessment. *Journal of Geophysical Research: Atmospheres*, *118*(11), 5380–5552. https://doi.org/10.1002/jgrd.50171

Boucher, O., Randall, D., Artaxo, P., Bretherton, C., Feingold, G., Forster, P., et al. (2013). IPCC AR5 Clouds and Aerosols. In *Climate Change 2013 - The Physical Science Basis* (pp. 571–658). Cambridge University Press, Cambridge, United Kingdom and New York, NY, USA. https://doi.org/10.1017/CBO9781107415324.016

Brito, J., Rizzo, L. V., Morgan, W. T., Coe, H., Johnson, B., Haywood, J., et al. (2014). Ground-based aerosol characterization during the South American Biomass Burning Analysis (SAMBBA) field experiment. *Atmospheric Chemistry and Physics*, *14*(22), 12069–12083. https://doi.org/10.5194/acp-14-12069-2014

Camponogara, G., Silva Dias, M. A. F., & Carrió, G. G. (2014). Relationship between Amazon biomass burning aerosols and rainfall over the La Plata Basin. *Atmospheric Chemistry and Physics*, *14*(9), 4397–4407. https://doi.org/10.5194/acp-14-4397-2014

Copernicus Climate Change Service (C3S) (2017). ERA5: Fifth generation of ECMWF atmospheric reanalyses of the global climate. Copernicus Climate Change Service Climate Data Store (CDS), Accessed January 2020. https://cds.climate.copernicus.eu/cdsapp#!/home

Dagan, G., Stier, P., Christensen, M., Cioni, G., Klocke, D., & Seifert, A. (2020). Atmospheric energy budget response to idealized aerosol perturbation in tropical cloud systems. *Atmospheric Chemistry and Physics*, *20*(7), 4523–4544. https://doi.org/10.5194/acp-20-4523-2020

Darbyshire, E., Morgan, W. T., Allan, J. D., Liu, D., Flynn, M. J., Dorsey, J. R., et al. (2019). The vertical distribution of biomass burning pollution over tropical South America from aircraft in situ measurements during SAMBBA. *Atmospheric Chemistry and Physics*, *19*(9), 5771–5790. https://doi.org/10.5194/acp-19-5771-2019

Edwards, J. M., & Slingo, A. (1996). Studies with a flexible new radiation code. I: Choosing a configuration for a large-scale model. *Quarterly Journal of the Royal Meteorological Society*, *122*(531), 689–719. https://doi.org/10.1256/smsqj.53106

Fan, J., Leung, L. R., Rosenfeld, D., Chen, Q., Li, Z., Zhang, J., & Yan, H. (2013). Microphysical effects determine macrophysical response for aerosol impacts on deep convective clouds. *Proceedings of the National Academy of Sciences of the United States of America*, *110*(48), E4581–E4590. https://doi.org/10.1073/pnas.1316830110

Fan, J., Rosenfeld, D., Zhang, Y., Giangrande, S. E., Li, Z., Machado, L. A. T., et al. (2018). Substantial

convection and precipitation enhancements by ultrafine aerosol particles. *Science*, *359*(6374), 411–418. https://doi.org/10.1126/science.aan8461
Feingold, G., Jiang, H., & Harrington, J. Y. (2005). On smoke suppression of clouds in Amazonia. *Geophysical Research Letters*, *32*(2), 1–4. https://doi.org/10.1029/2004GL021369
Gonçalves, W. A., Machado, L. A. T., & Kirstetter, P.-E. (2015). Influence of biomass aerosol on precipitation over the Central Amazon: an observational study. *Atmospheric Chemistry and Physics*, *15*(12), 6789–6800. https://doi.org/10.5194/acp-15-6789-2015
Gonzalez-Alonso, L., Val Martin, M., & Kahn, R. A. (2019). Biomass-burning smoke heights over the Amazon observed from space. *Atmospheric Chemistry and Physics*, *19*(3), 1685–1702. https://doi.org/10.5194/acp-19-1685-2019
Grabowski, W. W., & Morrison, H. (2016). Untangling microphysical impacts on deep convection applying a novel modeling methodology. Part II: Double-moment microphysics. *Journal of the Atmospheric Sciences*, *73*(9), 3749–3770. https://doi.org/10.1175/JAS-D-15-0367.1
Gryspeerdt, E., Quaas, J., Ferrachat, S., Gettelman, A., Ghan, S., Lohman, U., et al. (2017). Constraining the instantaneous aerosol influence on cloud albedo. *Proceedings of the National Academy of Sciences of the United States of America*, *114*(19), 4899–4904. https://doi.org/10.1073/pnas.1617765114
Herbert, R. J., Bellouin, N., Highwood, E. J., & Hill, A. A. (2020). Diurnal cycle of the semi-direct effect from a persistent absorbing aerosol layer over marine stratocumulus in large-eddy simulations. *Atmospheric Chemistry and Physics*, *20*(3), 1317–1340. https://doi.org/10.5194/acp-20-1317-2020
Herbert, R., Stier, P., Dagan, G. (2021). Data for submitted publication: "Isolating large-scale smoke impacts on cloud and precipitation processes over the Amazon with convection permitting resolution". http://doi.org/10.5281/zenodo.4445780
Hodzic, A., & Duvel, J. P. (2018). Impact of Biomass Burning Aerosols on the Diurnal Cycle of Convective Clouds and Precipitation Over a Tropical Island. *Journal of Geophysical Research: Atmospheres*, *123*(2), 1017–1036. https://doi.org/10.1002/2017JD027521
Ten Hoeve, J. E., Remer, L. A., & Jacobson, M. Z. (2011). Microphysical and radiative effects of aerosols on warm clouds during the Amazon biomass burning season as observed by MODIS: impacts of water vapor and land cover. *Atmospheric Chemistry and Physics*, *11*(7), 3021–3036. https://doi.org/10.5194/acp-11-3021-2011
Ten Hoeve, J. E., Remer, L. A., Correia, A. L., & Jacobson, M. Z. (2012). Recent shift from forest to savanna burning in the Amazon Basin observed by satellite. *Environmental Research Letters*, *7*(2), 024020. https://doi.org/10.1088/1748-9326/7/2/024020
Heikenfeld, M., White, B., Labbouz, L., & Stier, P. (2019). Aerosol effects on deep convection: the propagation of aerosol perturbations through convective cloud microphysics. *Atmospheric Chemistry and Physics*, *19*(4), 2601–2627. https://doi.org/10.5194/acp-19-2601-2019
Holanda, B. A., Pöhlker, M. L., Walter, D., Saturno, J., Sörgel, M., Ditas, J., et al. (2020). Influx of African biomass burning aerosol during the Amazonian dry season through layered transatlantic transport of black carbon-rich smoke. *Atmospheric Chemistry and Physics*, *20*(8), 4757–4785. https://doi.org/10.5194/acp-20-4757-2020
Holben, B. N., Tanré, D., Smirnov, A., Eck, T. F., Slutsker, I., Abuhassan, N., et al. (2001). An emerging ground-based aerosol climatology: Aerosol optical depth from AERONET. *Journal of Geophysical Research Atmospheres*, *106*(D11), 12067–12097. https://doi.org/10.1029/2001JD900014
Huffman, G. J., Stocker, E. F., Bolvin, D. T., Nelkin, E. J., & Tan, J. (2019). GES DISC Dataset: GPM IMERG Final Precipitation L3 Half Hourly 0.1 degree x 0.1 degree V06 (GPM_3IMERGHH 06). Retrieved July 9, 2020, from https://disc.gsfc.nasa.gov/datasets/GPM_3IMERGHH_06/summary
Iacono, M. J., Delamere, J. S., Mlawer, E. J., Shephard, M. W., Clough, S. A., & Collins, W. D. (2008). Radiative forcing by long-lived greenhouse gases: Calculations with the AER radiative transfer models. *Journal of Geophysical Research Atmospheres*, *113*(13). https://doi.org/10.1029/2008JD009944
Jiang, J. H., Su, H., Huang, L., Wang, Y., Massie, S., Zhao, B., et al. (2018). Contrasting effects on deep convective clouds by different types of aerosols. *Nature Communications*, *9*(1), 1–7. https://doi.org/10.1038/s41467-018-06280-4
Johnson, B. T., Shine, K. P., & Forster, P. M. (2004). The semi-direct aerosol effect: Impact of absorbing aerosols on marine stratocumulus. *Quarterly Journal of the Royal Meteorological Society*, *130*(599 PART B), 1407–1422. https://doi.org/10.1256/qj.03.61
Kaufman, Y. J., & Nakajima, T. (1993). Effect of Amazon smoke on cloud microphysics and albedo -

analysis from satellite imagery. *Journal of Applied Meteorology*, *32*(4), 729–744. https://doi.org/10.1175/1520-0450(1993)032<0729:EOASOC>2.0.CO;2
Khain, A., Rosenfeld, D., & Pokrovsky, A. (2005). Aerosol impact on the dynamics and microphysics of deep convective clouds. *Quarterly Journal of the Royal Meteorological Society*, *131*(611), 2639–2663. https://doi.org/10.1256/qj.04.62
Klocke, D., Brueck, M., Hohenegger, C., & Stevens, B. (2017, December 1). Rediscovery of the doldrums in storm-resolving simulations over the tropical Atlantic /704/106 /704/106/35 /704/106/35/823 perspective. *Nature Geoscience*. Nature Publishing Group. https://doi.org/10.1038/s41561-017-0005-4
Koren, I., Kaufman, Y. J., Remer, L. A., & Martins, J. V. (2004). Measurement of the Effect of Amazon Smoke on Inhibition of Cloud Formation. *Science*, *303*(5662), 1342–1345. https://doi.org/10.1126/science.1089424
Koren, I., Vanderlei Martins, J., Remer, L. A., & Afargan, H. (2008). Smoke invigoration versus inhibition of clouds over the amazon. *Science*, *321*(5891), 946–949. https://doi.org/10.1126/science.1159185
Lebo, Z. (2018). A numerical investigation of the potential effects of aerosol-induced warming and updraft width and slope on updraft intensity in deep convective clouds. *Journal of the Atmospheric Sciences*, *75*(2), 535–554. https://doi.org/10.1175/JAS-D-16-0368.1
Lee, S. S., Feingold, G., McComiskey, A., Yamaguchi, T., Koren, I., Vanderlei Martins, J., & Yu, H. (2014). Effect of gradients in biomass burning aerosol on shallow cumulus convective circulations. *Journal of Geophysical Research: Atmospheres*, *119*(16), 9948–9964. https://doi.org/10.1002/2014JD021819
Leuenberger, D., Koller, M., Fuhrer, O., & Schär, C. (2010). A generalization of the SLEVE vertical coordinate. *Monthly Weather Review*, *138*(9), 3683–3689. https://doi.org/10.1175/2010MWR3307.1
Liu, L., Cheng, Y., Wang, S., Wei, C., Pöhlker, M., Pöhlker, C., et al. (2020). Impact of biomass burning aerosols on radiation, clouds, and precipitation over the Amazon during the dry season: dependence of aerosol-cloud and aerosol-radiation interactions on aerosol loading. *Atmospheric Chemistry and Physics*, 1–50. https://doi.org/10.5194/acp-2020-191
Lovejoy, T. E., & Nobre, C. (2019, December 20). Amazon tipping point: Last chance for action. *Science Advances*. American Association for the Advancement of Science. https://doi.org/10.1126/sciadv.aba2949
Malavelle, F. F., Haywood, J. M., Mercado, L. M., Folberth, G. A., Bellouin, N., Sitch, S., & Artaxo, P. (2019). Studying the impact of biomass burning aerosol radiative and climate effects on the Amazon rainforest productivity with an Earth system model. *Atmospheric Chemistry and Physics*, *19*(2), 1301–1326. https://doi.org/10.5194/acp-19-1301-2019
Martin, S. T., Artaxo, P., Machado, L. A. T., Manzi, A. O., Souza, R. A. F., Schumacher, C., et al. (2016). Introduction: Observations and Modeling of the Green Ocean Amazon (GoAmazon2014/5). *Atmospheric Chemistry and Physics*, *16*(8), 4785–4797. https://doi.org/10.5194/acp-16-4785-2016
Martins, J. A., Silva Dias, M. A. F., & Gonçalves, F. L. T. (2009). Impact of biomass burning aerosols on precipitation in the Amazon: A modeling case study. *Journal of Geophysical Research*, *114*(D2). https://doi.org/10.1029/2007jd009587
Mlawer, E. J., Taubman, S. J., Brown, P. D., Iacono, M. J., & Clough, S. A. (1997). Radiative transfer for inhomogeneous atmospheres: RRTM, a validated correlated-k model for the longwave. *Journal of Geophysical Research Atmospheres*, *102*(14), 16663–16682. https://doi.org/10.1029/97jd00237
Morton, D. C., Defries, R. S., Randerson, J. T., Giglio, L., Schroeder, W., & van der Werf, G. R. (2008). Agricultural intensification increases deforestation fire activity in Amazonia. *Global Change Biology*, *14*(10), 2262–2275. https://doi.org/10.1111/j.1365-2486.2008.01652.x
Nobre, C. A., Sampaio, G., Borma, L. S., Castilla-Rubio, J. C., Silva, J. S., & Cardoso, M. (2016). Land-use and climate change risks in the amazon and the need of a novel sustainable development paradigm. *Proceedings of the National Academy of Sciences of the United States of America*, *113*(39), 10759–10768. https://doi.org/10.1073/pnas.1605516113
de Oliveira, G., Chen, J. M., Mataveli, G. A. V., Chaves, M. E. D., Seixas, H. T., da Cardozo, F. S., et al. (2020). Rapid recent deforestation incursion in a vulnerable indigenous land in the Brazilian Amazon and fire-driven emissions of fine particulate aerosol pollutants. *Forests*, *11*(8), 829. https://doi.org/10.3390/f11080829
Oliveira, R., Maggioni, V., Vila, D., & Morales, C. (2016). Characteristics and Diurnal Cycle of GPM Rainfall Estimates over the Central Amazon Region. *Remote Sensing*, *8*(7), 544.

https://doi.org/10.3390/rs8070544
Polonik, P., Knote, C., Zinner, T., Ewald, F., Kölling, T., Mayer, B., et al. (2020). The challenge of simulating the sensitivity of the Amazonian cloud microstructure to cloud condensation nuclei number concentrations. *Atmospheric Chemistry and Physics*, *20*(3), 1591–1605. https://doi.org/10.5194/acp-20-1591-2020
Reddington, C. L., Morgan, W. T., Darbyshire, E., Brito, J., Coe, H., Artaxo, P., et al. (2019). Biomass burning aerosol over the Amazon: analysis of aircraft, surface and satellite observations using a global aerosol model. *Atmospheric Chemistry and Physics*, *19*(14), 9125–9152. https://doi.org/10.5194/acp-19-9125-2019
Rosenfeld, D., Lohmann, U., Raga, G. B., O'Dowd, C. D., Kulmala, M., Fuzzi, S., et al. (2008). Flood or drought: How do aerosols affect precipitation? *Science*. American Association for the Advancement of Science. https://doi.org/10.1126/science.1160606
Rothenberg, D., Avramov, A., & Wang, C. (2018). On the representation of aerosol activation and its influence on model-derived estimates of the aerosol indirect effect. *Atmospheric Chemistry and Physics*, *18*(11), 7961–7983. https://doi.org/10.5194/acp-18-7961-2018
Schafer, J. S., Eck, T. F., Holben, B. N., Artaxo, P., & Duarte, A. F. (2008). Characterization of the optical properties of atmospheric aerosols in Amazônia from long-term AERONET monitoring (1993-1995 and 1999-2006). *Journal of Geophysical Research Atmospheres*, *113*(4). https://doi.org/10.1029/2007JD009319
Schrodin, E., & Heise, E. (2002, February). A New Multi-Layer Soil Model. *COSMO Newsletter*, pp. 149–151.
Seifert, A., & Beheng, K. D. (2006). A two-moment cloud microphysics parameterization for mixed-phase clouds. Part 2: Maritime vs. continental deep convective storms. *Meteorology and Atmospheric Physics*, *92*(1–2), 67–82. https://doi.org/10.1007/s00703-005-0113-3
Simpson, E., Connolly, P., & McFiggans, G. (2014). An investigation into the performance of four cloud droplet activation parameterisations. *Geoscientific Model Development*, *7*(4), 1535–1542. https://doi.org/10.5194/gmd-7-1535-2014
Stevens, B., Fiedler, S., Kinne, S., Peters, K., Rast, S., Müsse, J., et al. (2017). MACv2-SP: a parameterization of anthropogenic aerosol optical properties and an associated Twomey effect for use in CMIP6. *Geoscientific Model Development*, *10*(1), 433–452. https://doi.org/10.5194/gmd-10-433-2017
Stocker, T. F., Qin, D., Plattner, G.-K., Tignor, M., Allen, S. K., Boschung, J., et al. (2013). AR5 Climate Change 2013: The Physical Science Basis — IPCC. Retrieved February 18, 2019, from https://www.ipcc.ch/report/ar5/wg1/
Thornhill, G. D., Ryder, C. L., Highwood, E. J., Shaffrey, L. C., & Johnson, B. T. (2018). The effect of South American biomass burning aerosol emissions on the regional climate. *Atmospheric Chemistry and Physics*, *18*(8), 5321–5342. https://doi.org/10.5194/acp-18-5321-2018
Wendisch, M., Poschl, U., Andreae, M. O., MacHado, L. A. T., Albrecht, R., Schlager, H., et al. (2016). Acridicon-chuva campaign: Studying tropical deep convective clouds and precipitation over amazonia using the New German research aircraft HALO. *Bulletin of the American Meteorological Society*, *97*(10), 1885–1908. https://doi.org/10.1175/BAMS-D-14-00255.1
Wu, L., Su, H., & Jiang, J. H. (2011). Regional simulations of deep convection and biomass burning over South America: 2. Biomass burning aerosol effects on clouds and precipitation. *Journal of Geophysical Research Atmospheres*, *116*(17). https://doi.org/10.1029/2011JD016106
Xue, H., Feingold, G., & Stevens, B. (2008). Aerosol effects on clouds, precipitation, and the organization of shallow cumulus convection. *Journal of the Atmospheric Sciences*, *65*(2), 392–406. https://doi.org/10.1175/2007JAS2428.1
Yin, L., Fu, R., Shevliakova, E., & Dickinson, R. E. (2013). How well can CMIP5 simulate precipitation and its controlling processes over tropical South America? *Climate Dynamics*, *41*(11–12), 3127–3143. https://doi.org/10.1007/s00382-012-1582-y
Yu, H., Fu, R., Dickinson, R. E., Zhang, Y., Chen, M., & Wang, H. (2007). Interannual variability of smoke and warm cloud relationships in the Amazon as inferred from MODIS retrievals. *Remote Sensing of Environment*, *111*(4), 435–449. https://doi.org/10.1016/j.rse.2007.04.003
Zängl, G., Reinert, D., Rípodas, P., & Baldauf, M. (2015). The ICON (ICOsahedral Non-hydrostatic) modelling framework of DWD and MPI-M: Description of the non-hydrostatic dynamical core.

Quarterly Journal of the Royal Meteorological Society, *141*(687), 563–579. https://doi.org/10.1002/qj.2378

Zhang, Y., Fu, R., Yu, H., Dickinson, R. E., Juarez, R. N., Chin, M., & Wang, H. (2008). A regional climate model study of how biomass burning aerosol impacts land-atmosphere interactions over the Amazon. *Journal of Geophysical Research*, *113*(D14). https://doi.org/10.1029/2007jd009449

Zhang, Y., Fu, R., Yu, H., Qian, Y., Dickinson, R., Silva Dias, M. A. F., et al. (2009). Impact of biomass burning aerosol on the monsoon circulation transition over Amazonia. *Geophysical Research Letters*, *36*(10), L10814. https://doi.org/10.1029/2009GL037180